

The redshift-evolution of the distribution of star formation among dark matter halos as seen in the infrared

Matthieu Béthermin¹, Lingyu Wang², Olivier Doré^{3,4}, Guilaïne Lagache⁵, Mark Sargent¹, Emanuele Daddi¹, Morgane Cousin⁵, and Hervé Aussel¹

¹ Laboratoire AIM-Paris-Saclay, CEA/DSM/Irfu - CNRS - Université Paris Diderot, CEA-Saclay, pt courrier 131, F-91191 Gif-sur-Yvette, France, email: matthieu.bethermin@cea.fr

² Computational Cosmology, Department of Physics, University of Durham, South Road, Durham, DH1 3LE, UK

³ Jet Propulsion Laboratory, California Institute of Technology, 4800 Oak Grove Drive, Pasadena, California, U.S.A

⁴ California Institute of Technology, MC249-17, Pasadena, CA 91125 USA

⁵ Institut d'Astrophysique Spatiale, CNRS (UMR8617) Université Paris-Sud 11, Bâtiment 121, Orsay, France

Received ??? / Accepted ???

ABSTRACT

Recent studies revealed a strong correlation between the star formation rate (SFR) and stellar mass of the majority of star-forming galaxies, the so-called star-forming main sequence. An empirical modeling approach (the 2-SFM framework) which distinguishes between the main sequence and rarer starburst galaxies is capable of reproducing most statistical properties of infrared galaxies, such as number counts, luminosity functions, and redshift distributions. In this paper, we extend this approach by establishing a connection between stellar mass and halo mass with the technique of abundance matching. Based on a few, simple assumptions and a physically motivated formalism, our model successfully predicts the (cross-)power spectra of the cosmic infrared background (CIB), the cross-correlation between CIB and cosmic microwave background (CMB) lensing, and the correlation functions of bright, resolved infrared galaxies measured by *Herschel*, *Planck*, ACT and SPT. We use this model to infer the redshift distribution of CIB-anisotropies and of the CIBx CMB lensing signal, as well as the level of correlation between CIB-anisotropies at different wavelengths. We study the link between dark matter halos and star-forming galaxies in the framework of our model. We predict that more than 90% of cosmic star formation activity occurs in halos with masses between $10^{11.5}$ and $10^{13.5} M_{\odot}$. Taking into account subsequent mass growth of halos, this implies that the majority of stars were initially (at $z > 3$) formed in the progenitors of clusters ($M_h(z=0) > 10^{13.5} M_{\odot}$), then in groups ($10^{12.5} < M_h(z=0) < 10^{13.5} M_{\odot}$) at $0.5 < z < 3$ and finally in Milky-Way-like halos ($10^{11.5} < M_h(z=0) < 10^{12.5} M_{\odot}$) at $z < 0.5$. At all redshifts, the dominant contribution to the star formation rate density stems from halos of mass $\sim 10^{12} M_{\odot}$, in which the instantaneous star formation efficiency – defined here as the ratio between SFR and baryonic accretion rate – is maximal ($\sim 70\%$). The strong redshift-evolution of SFR in the galaxies that dominate the CIB is thus plausibly driven by increased accretion from the cosmic web onto halos of this characteristic mass scale. Material (effective spectral energy distributions, differential emissivities of halos, relations between M_h and SFR) associated to this model is available at <http://irfu.cea.fr/Sap/Phoea/Page/index.php?id=537>.

Key words. Galaxies: star formation – Galaxies: halos – Galaxies: statistics – Cosmology: diffuse radiation – Cosmology: dark matter – Submillimeter: galaxies

1. Introduction

A detailed understanding of galaxy formation in the cosmological context is one of the main problems of modern astrophysics. The star formation rate (SFR) of galaxies across cosmic time is one of the key observables to understand their evolution. However, measurements of SFR are difficult, because most of the UV light emitted by young massive stars is absorbed by interstellar dust. This light is re-radiated in the infrared between $6\mu\text{m}$ and 1mm . The cosmic infrared background (CIB), detected for the first time in FIRAS data (Puget et al. 1996; Fixsen et al. 1998; Hauser et al. 1998), is the relic of all dust emissions since the recombination. It is the strongest background after the cosmic microwave background (CMB) and contains half of the energy emitted after recombination (Hauser & Dwek 2001; Dole et al. 2006). Identifying the sources responsible for this background and their physical properties is thus crucial to understanding the star formation history in the Universe. Unfortunately, because of the confusion caused by the limited resolution of the current infrared/millimeter facilities (Condon 1974; Dole et al.

2004), only a small fraction of this background can be directly resolved into individual sources at wavelengths longer than $250\mu\text{m}$ (Oliver et al. 2010; Béthermin et al. 2012c), where the CIB becomes dominated by $z > 1$ sources (Lagache et al. 2003, 2005; Béthermin et al. 2011, 2012c). We thus have to study the statistical properties of the unresolved background, if we want to unveil the infrared properties of galaxies which host the bulk of the obscured star formation at high redshift.

We can use statistical tools to measure the photometric properties of galaxies emitting the CIB. P(D) analysis (Condon 1974; Patanchon et al. 2009) is a method measuring the flux distribution of sources below the confusion limit by considering only the pixel histogram of an infrared/millimeter map. Glenn et al. (2010) managed to measure the number counts (flux distribution) of SPIRE sources down to one order of magnitude below the confusion limit using P(D) and resolve $\sim 2/3$ of the CIB into individual sources. Strong constraints on contributions to the CIB were also derived by stacking analyses (Dole et al.

2006; Marsden et al. 2009). This method allows to measure the mean flux of a population individually detected at a shorter wavelength¹ but not in the far-infrared/millimeter, by stacking of cutout images centered on short-wavelength detections. Number counts below the confusion limit were measured with a method based on stacking (Béthermin et al. 2010a,b). In addition to this, Béthermin et al. (2012c) also measured counts per redshift slice using an input catalog containing both $24\mu\text{m}$ fluxes and redshifts and a complex reconstruction of the counts based on stacking. These analyses provided constraints on the CIB redshift distribution. Nevertheless, an empirical model is still necessary to deduce the obscured star formation history from number counts at various wavelengths (e.g. Le Borgne et al. 2009; Valiante et al. 2009; Franceschini et al. 2010; Béthermin et al. 2011; Marsden et al. 2011; Rahmati & van der Werf 2011; Lapi et al. 2011; Gruppioni et al. 2011).

Large scale CIB anisotropies measured by *Spitzer* (Lagache et al. 2007; Grossan & Smoot 2007; Pénin et al. 2012b), *BLAST* (Viero et al. 2009), the South Pole Telescope (SPT, Hall et al. 2010), *Herschel* (Amblard et al. 2011; Viero et al. 2012) and *Planck* (Planck Collaboration et al. 2011) also provide degenerate constraints on the evolution of infrared-galaxy emissivities and the link between infrared galaxies and dark matter halos. This degeneracy can be broken combining anisotropy information with infrared number counts (see above). The first generation of models used to predict/interpret CIB anisotropies was based on a combination of an evolutionary model of emissivities of infrared galaxies and a linear bias or a halo occupation distribution (HOD) model describing the spatial distribution of galaxies (Knox et al. 2001; Lagache et al. 2007; Amblard & Cooray 2007; Viero et al. 2009; Hall et al. 2010; Planck Collaboration et al. 2011; Amblard et al. 2011; Pénin et al. 2012a; Xia et al. 2012). The emissivities are deduced from a model of galaxy evolution (e.g. Béthermin et al. 2011; Lapi et al. 2011) or represented by a simple parametric function (Hall et al. 2010; Amblard et al. 2011). However, these models assume that there is no dependency between clustering and luminosity and in general a single HOD or linear bias for all redshifts. Consequently, these models have difficulties to fit all wavelengths simultaneously. Shang et al. (2012) proposed a new approach assuming an infrared-light-to-mass ratio which varies with halo mass and redshift (see also the De Bernardis & Cooray 2012 approach focused only on $250\mu\text{m}$). This new model is also able to roughly reproduce the number counts (LFs respectively), though their description of infrared galaxies is simplistic (a single SED for all galaxies at all redshifts, no scatter on the mass-to-light ratio). Another approach was proposed by Addison et al. (2012), who combine a backward-evolution counts model very similar to the Béthermin et al. (2011) approach and a scale-dependent effective bias of infrared galaxies to predict the CIB power spectrum. This simplified approach is very efficient in fitting the data, but is purely descriptive and provides little information on the physical link between galaxies and dark matter halos.

In this paper, we propose a new approach to model both CIB anisotropies and galaxy number counts based on the observed relation between physical properties in galaxies and their evolution with redshift. We use the stellar mass (M_\star) as a gateway

to link the halo mass (M_h) and star formation rate (SFR). The stochastic link between SFR and M_\star is modeled following the Béthermin et al. (2012a) model (hereafter B12), which is based on the observation of a main-sequence (MS) of star-forming galaxies (i.e. a strong correlation between stellar mass and star formation rate SFR evolving with redshift, Noeske et al. 2007; Elbaz et al. 2007; Daddi et al. 2007; Rodighiero et al. 2011) and provides one of the best fits of mid-infrared-to-radio number counts. It contains two types of star-forming galaxies with different spectral energy distributions (SEDs): secularly star-forming MS galaxies and a population of episodic, probably merger-driven starbursts with a strong excess of SFR compared to the main sequence following the 2 star formation modes (2SFM) formalism introduced in Sargent et al. (2012). The relation between stellar and halo mass is derived by abundance matching (Vale & Ostriker 2004; Conroy & Wechsler 2009; Behroozi et al. 2010) assuming a monotonic relation without scatter between these quantities. Béthermin et al. (2012b) used this technique to connect SFR and M_h for MS galaxies in a qualitative way (see also Wang et al. 2012). This paper improves and extends the approach of Béthermin et al. (2012b) in order to predict the anisotropy of the CIB and the clustering of infrared galaxies. This new formalism also permits us to describe in a phenomenological way the quenching of star-formation in massive galaxies and their satellites and involves a refined treatment of sub-halos.

In Sect. 2, we present the philosophy of our approach. In Sect. 3, we detail the ideas on which our model is based, and especially how we assign infrared properties to galaxies hosted by a dark matter halo. In Sect. 4 and 5, we describe the formalism used to compute the power-spectrum of CIB anisotropies and angular correlation functions of infrared galaxies, respectively. In Sect. 6, we present the results of our modeling and an extensive comparison with observations. In Sect. 7, we discuss the successes, but also the limitation of our model. In Sect. 8, we detail the properties of the CIB predicted a posteriori by our model, such as redshift distribution or correlation between bands. In Sect. 9, we discuss how the history of star formation history proceeds depending on the mass of dark matter halos. We conclude in Sect. 10. In Appendix A, we provide tables of conversion from multipole ℓ to angle θ and from frequencies to wavelengths, as we use both conventions interchangeably in the paper.

In this paper, we assume a WMAP-7 cosmology (Larson et al. 2010) and a Chabrier (2003) initial mass function.

2. Philosophy of our approach

The majority of previous CIB models were purely phenomenological and describe the emissivity and clustering of infrared galaxies using a large set of free parameters. This approach is useful to derive quantities such as, e.g. the mass where star formation is most efficient. However, it is sometimes hard to test the validity of these models as a good fit can be easily obtained considering their number of free parameters. Kim et al. (2012) proposed a physical approach based on a semi-analytical galaxy formation model, which unfortunately have substantial discrepancies with the data. We propose an alternative phenomenological approach, which represents an intermediate solution between a fully empirical and a physical model. We

¹ $24\mu\text{m}$ is often used because $\sim 80\%$ of the background is resolved into sources at this wavelength (Papovich et al. 2004; Béthermin et al. 2010a).

minimize the number of free parameters and build our analysis on the observed relation between physical quantities (e.g. the specific star formation rate in main-sequence galaxies calibrated from optical, near-infrared, far-infrared and radio data). We thus do not aim to fine tune the various parameters of the model, but to test if the scaling-laws measured from external datasets (measurements on small samples extrapolated to all galaxies, optical/near-infrared measurements of stellar mass or SFR) are compatible with the data under different scenarios. For this reason, we choose an approach based on abundance matching with no free parameters to describe the link between stellar mass and halo mass and use the B12 model, which follows the same philosophy to link infrared properties and stellar mass.

3. Connecting star formation and halo mass by abundance matching

In this section, we describe how we stochastically assign properties of star formation to galaxies as a function of the host halo mass, combining prescriptions from several modeling works. In Sect. 3.1 and 3.2, we present the halo and stellar mass functions used in this paper. We then describe how we connect stellar and halo mass by abundance matching in Sect. 3.3. Sect. 3.4 describes how we stochastically attribute a star-formation rate from the stellar mass using recipes based on the B12 model. Finally, we describe how we deduce infrared properties of the galaxies from their physical properties in Sect. 3.5 using the B12 model.

3.1. Halo mass function

In our analysis, we used the halo mass function (HMF) of Tinker et al. (2008) (in our notation $\frac{d^2N}{d\log(M_h)dV}$). We choose halo mass (M_h) to be defined by an overdensity of $\Delta = 200$ (often called M_{200}). This HMF evolves with redshift and was calibrated on N-body simulations. We also need the mass function of sub-halos, which are supposed to host satellite galaxies. The one we adopt here comes from Tinker & Wetzel (2010), and provides the mass distribution of sub-halos in a parent halo of total mass M_h :

$$\frac{dN}{d\log(m_{\text{sub}}) \times \ln(10)}(m_{\text{sub}}|M_h) = 0.30 \times \left(\frac{m_{\text{sub}}}{M_h}\right)^{-0.7} \times \exp\left(-9.9 \left(\frac{m_{\text{sub}}}{M_h}\right)^{2.5}\right), \quad (1)$$

where m_{sub} is the sub-halo mass. In our analysis we neglect sub-structures inside sub-halos. The mass function of sub-halos is thus

$$\frac{d^2N}{d\log(m_{\text{sub}})dV}(m_{\text{sub}}) = \int_0^{M_h} \frac{dN}{d\log(m_{\text{sub}})}(m_{\text{sub}} = \mathcal{M}_h|M_h) \times \frac{d^2N}{d\log(M_h)dV}d\log M_h, \quad (2)$$

We also introduce a pseudo "total" mass function, given by the sum of the mass functions of halos and sub-halos:

$$\frac{d^2N}{d\log(\mathcal{M}_h)dV}(\mathcal{M}_h) = \frac{d^2N}{d\log(M_h)dV}(M_h = \mathcal{M}_h) + \frac{d^2N}{d\log(m_{\text{sub}})dV}(m_{\text{sub}} = \mathcal{M}_h). \quad (3)$$

Here \mathcal{M}_h may stand for either the total mass of a halo (M_h) for a main structure or the mass of the sub-halo for a sub-structure (m_{sub}). This function will be useful for our abundance matching procedure presented Sect 3.3, because we will assume that the properties of galaxies are linked with \mathcal{M}_h . However, this is not exactly a mass function, because sub-halos are counted twice, namely both in the total mass function and in the sub-halo mass function. Fig. 1 (left-hand column) shows the contribution of main and sub-halos at $z \sim 0.5$. The majority of high-mass halos are main-halos, while a large fraction of low-mass halos are sub-structures of more massive halos. At $\mathcal{M}_h = 10^{12} M_\odot$, $\sim 1/3$ of halos are sub-halos of more massive halos.

3.2. Stellar mass function

We used the same stellar mass function (SMF) of star-forming galaxies as B12, in order to be consistent with this model which is used to link the stellar mass to the infrared properties (see Sect. 3.4). This mass function is parametrized by an evolving Schechter (1976) function:

$$\phi = \frac{dN}{d\log(M_\star)} = \phi_b(z) \times \left(\frac{M_\star}{M_b}\right)^{-\alpha_{MF}} \times \exp\left(-\frac{M_\star}{M_b}\right) \times \frac{M_\star}{M_b} \ln(10), \quad (4)$$

with a redshift-invariant characteristic mass M_b and faint-end slope α_{MF} . ϕ_b , the characteristic density, is constant between $z=0$ and $z=1$ but decreases at $z>1$ as

$$\log(\phi_b) = \log(\phi_b)(z < 1) + \gamma_{SFMF}(1 - z). \quad (5)$$

The various parameters were chosen to reproduce the observed evolution of the mass function of star-forming galaxies. Their values are given in B12.

In order to correctly populate dark matter halos, we also need to account for the population of non-star-forming galaxies (called quenched galaxies hereafter), which are essentially red, passively-evolving, elliptical galaxies below the main sequence. Star formation activity in these objects is weak and this population was thus ignored in the B12 model because of their negligible infrared emission. These galaxies however contribute significantly to the mass function at high mass (e.g. Ilbert et al. 2013, see Fig. 1 upper right panel) and thus are generally the kind of galaxy that is encountered in massive halos. We used the mass function of quiescent galaxies from Ilbert et al. (2010) at $z < 2$ and Ilbert et al. (2013) at $z > 2$, fitted by a Schechter (1976) function. $\log(\phi_b)$, $\log(M_b)$, and α are interpolated between the center of each redshift bins and extrapolated at $z > 3$. The total mass function (showed Fig. 1 upper right panel) is the sum of the contribution of both quenched and star-forming galaxies. The fraction of quenched galaxies at a given stellar mass and redshift is called $q(M_\star, z)$. The upper right panel of Fig. 1 shows the mass function and its decomposition into quenched and star-forming galaxies. The lower right panel shows the fraction of quenched galaxies as a function of stellar mass. At high mass ($M_\star > 10^{11} M_\odot$) and low redshift ($z < 1$), the majority of galaxies are quenched, when the other regimes are dominated by star-forming galaxies.

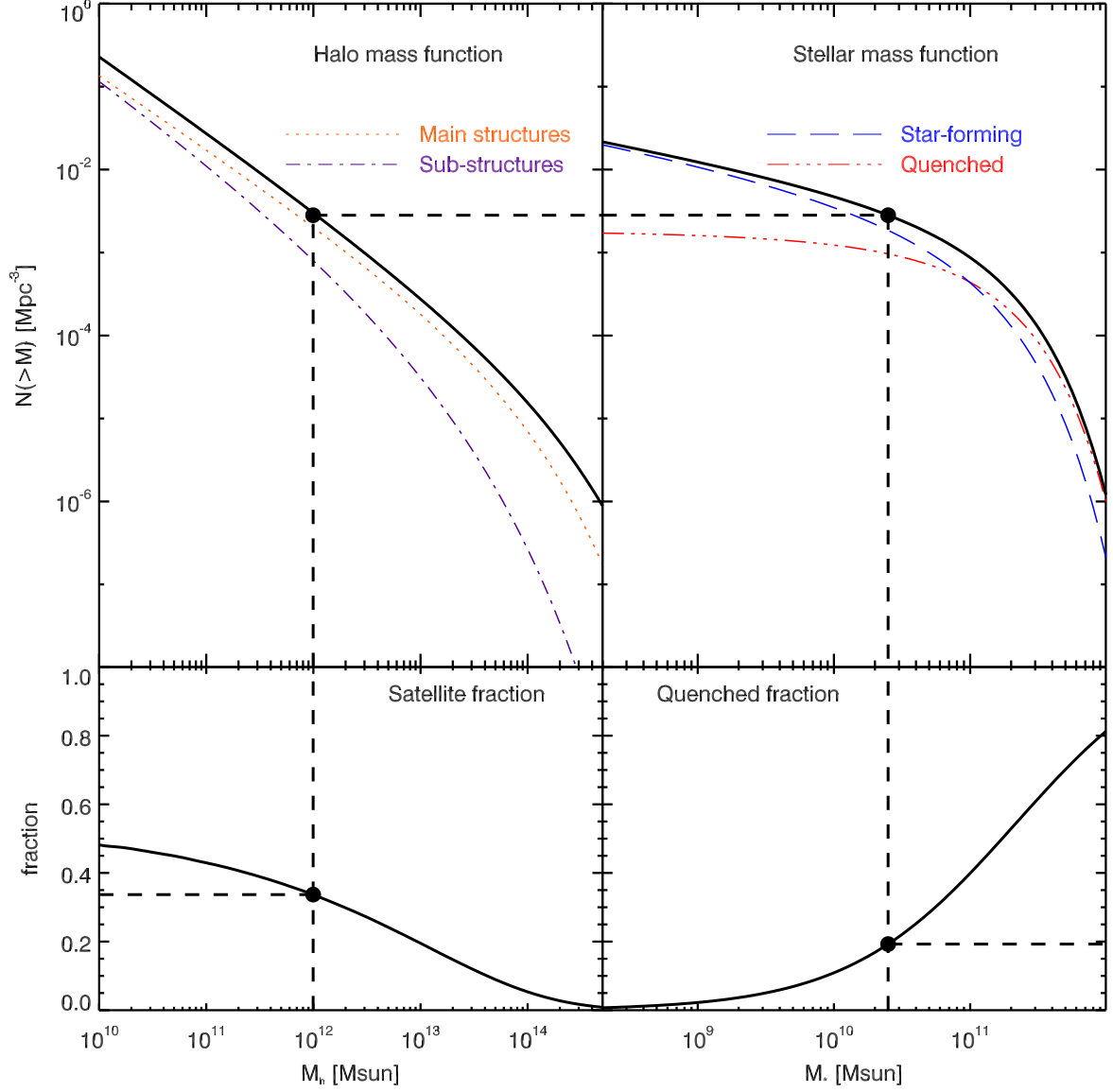


Fig. 1. Illustration of the method used to connect various quantities by abundance matching as described in Sect. 3.3. The dashed line illustrates the connection between various quantities. We arbitrarily chose to plot results at $z = 0.5$. *Upper left panel:* integral HMF and contribution of main halos (dotted orange line) and sub-halos (dot-dash purple line). *Upper right panel:* integral SMF and contribution of star-forming (long-dashed blue line) and quenched (three-dot-dash red line). *Lower left panel:* variation with halo mass of the fraction of halos that are sub-halos. *Lower right panel:* fraction of quenched galaxies as a function of stellar mass.

3.3. Connecting stellar mass and halo mass through abundance matching

The abundance matching technique is based on the hypothesis of a monotonic link between two quantities. This is a fair assumption for the link between the stellar and halo mass of a central galaxy at a given redshift (More et al. 2009; Moster et al. 2010; Behroozi et al. 2010). In this work, we will follow Behroozi et al. (2010) and Watson & Conroy (2013) and assume that sub-halos and main-halos follow the same M_\star - M_h relation. Under this assumption, we associate halo mass to a stellar mass by putting the n -th most massive galaxy (in term of stellar mass) into the n -th most massive halo. In practice, we do not use catalogues, but analytic mass functions. The non-parametric function linking stellar and halo mass ($M_\star = f(M_h)$) is thus the

solution of the implicit equation

$$n_{M_\star}(> f(M_h) = M_\star) = n_{M_h}, \quad (6)$$

where $n_{M_\star}(> M_\star)$ is the number density (in comoving units) of galaxies more massive than M_\star (i.e. the integral of the mass function), and n_{M_h} the equivalent for halo mass. We can thus associate halo mass to stellar mass by taking the halo mass at which the number density of galaxies and halos are the same, as illustrated by Fig. 1 (upper panels).

In this approach, we neglect the effect of the scatter on the stellar-to-halo-mass ratio, which would further complicate our analysis of CIB anisotropies. This induces a bias on the estimation of f . However, this effect is smaller than the statistical uncertainties for $M_h > 10^{14.5} M_\odot$ (Behroozi et al. 2010), which host mainly passive galaxies (see Fig. 1). The

scatter around f could also induce a bias on the estimate of the observables as the CIB anisotropies. However, the large-scale anisotropies are sensitive to the mean emissivity of galaxies and are not affected by the scatter. The small-scale Poisson term can be computed directly from counts model without assumptions on the dark matter (see Sect. 4). The angular correlation of bright resolved galaxies can be affected by the scatter on halo mass, but the scatter between stellar and halo mass (~ 0.15 dex) has the same order of magnitude as the scatter between stellar mass and star formation rate, which is taken into account by our model (~ 0.15 - 0.2 dex). The impact of the scatter of the stellar mass-halo mass relation on the correlation function is thus expected to be relatively small.

3.4. Connecting star formation rate to stellar mass

In the previous section, we explained how we can assign a stellar mass to a galaxy knowing its halo mass. Unfortunately, we cannot link star formation rate to stellar mass by abundance matching assuming a monotonic relation. This hypothesis is only valid for main-sequence galaxies, but not for quenched, for which $\text{sSFR} \ll \text{sSFR}_{\text{MS}}$, where sSFR is the specific star formation rate i.e. SFR/M_\star and sSFR_{MS} the typical value of this parameter in main-sequence galaxies, and starburst galaxies, for which $\text{sSFR} \gg \text{sSFR}_{\text{MS}}$. For quenched galaxies, we neglect the star-formation and thus take $\text{SFR} = 0 \text{ M}_\odot \text{ yr}^{-1}$ for simplicity. For star-forming galaxies (main-sequence and starburst), we assume that SFR follows a double log-normal distribution at fixed redshift and stellar mass (Sargent et al. 2012, B12):

$$p(\log(\text{SFR})|M_\star, z) \propto p_{\text{MS}} + p_{\text{SB}} \\ \propto \exp\left(-\frac{(\log(\text{SFR}) - \log(\text{sSFR}_{\text{MS}} \times M_\star))^2}{2\sigma_{\text{MS}}^2}\right) \\ + r_{\text{SB}} \times \exp\left(-\frac{(\log(\text{SFR}) - \log(\text{sSFR}_{\text{MS}} \times M_\star) - B_{\text{SB}})^2}{2\sigma_{\text{SB}}^2}\right). \quad (7)$$

The first term describes the sSFR distribution of main-sequence galaxies (p_{MS}), and the second one that of starbursts (p_{SB}). Star formation in starburst is boosted on average by a factor B_{SB}^2 . σ_{MS} and σ_{SB} are the dispersion around the central values. The evolution of the main-sequence parametrized as in B12:

$$\text{sSFR}_{\text{MS}}(z, M_\star) = \text{sSFR}_{\text{MS},0} \times \left(\frac{M_\star}{10^{11} \text{ M}_\odot}\right)^{\beta_{\text{MS}}} \\ \times (1 + \min(z, z_{\text{evo}}))^{\gamma_{\text{MS}}}. \quad (8)$$

The starburst ratio r_{SB} (i.e. the relative normalization of the two log-normal distributions) is also provided by the B12 model:

$$r_{\text{SB}}(z) = r_{\text{SB},0} \times (1 + \min(z, z_{\text{SB}}))^{\gamma_{\text{SB}}}, \text{ where } z_{\text{SB}} = 1. \quad (9)$$

The values of the parameters in our base model (model A) are the ones provided in B12³. We also used a second version of the model (model B) for which the high redshift trend was

² A detailed discussion of the SFR-enhancements of starbursts and their description in the 2-SFM framework is provided in Sargent et al. (2013).

³ Parameters provided in B12 are given assuming a Salpeter (1955) IMF when this paper assumes a Chabrier (2003) IMF. A correction of 0.24 dex have thus to be applied to some of the parameters to take into account this difference of IMF.

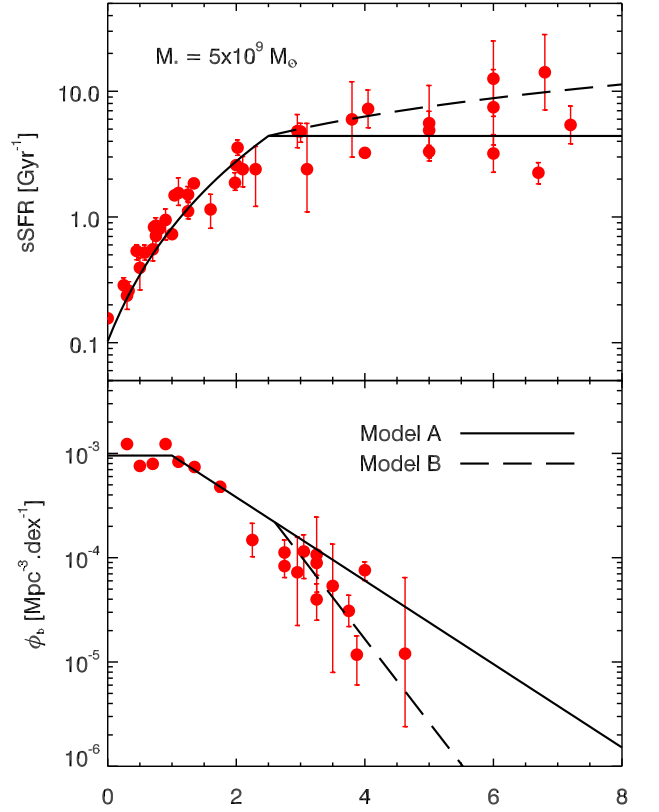


Fig. 2. Upper panel: Evolution of specific star formation rate in main-sequence galaxies of $5 \times 10^9 \text{ M}_\odot$. Lower panel: Evolution of the characteristic mass ϕ_b of the mass function with redshift. Both panel: model A (B12 model) is represented with a solid line and model B (modified version with higher sSFR and lower density at high redshift) with a long-dashed line.

slightly modified, following the findings of a slowly increasing sSFR at high redshift (Stark et al. 2012; de Barros et al. 2012; Gonzalez et al. 2012). These higher values are the consequence of an improved modeling of the contribution of nebular line emissions to flux in near-infrared broad-band filters. For this modified version, we assume an evolution of sSFR at $z > 2.5$ in $(1+z)$. In order to avoid an overprediction of bright millimeter counts, we compensate this increase of sSFR by a quicker decrease of the characteristic density of the stellar mass function in the same redshift range ($(1+z)^{-0.8}$ instead of $(1+z)^{-0.4}$), thus keeping the same number of bright objects. As shown in Fig. 2, both these scenarios are compatible with the data, because of the large scatter on the measurements. In Sect. 6 and 7, we discuss which scenario is actually favored by infrared observations.

3.5. Infrared outputs of galaxies

In massive galaxies, the bulk of the UV light coming from young stars is absorbed by dust and re-emitted in the infrared. We can thus assume that the bolometric infrared (8-1000 μm) luminosity L_{IR} is proportional to star formation rate (Kennicutt 1998, the conversion factor is $K = \text{SFR}/L_{\text{IR}} = 1 \times 10^{-10} \text{ M}_\odot \text{ yr}^{-1} L_\odot^{-1}$ if we assume a Chabrier (2003) IMF). In low-mass galaxies, a significant part of the UV light escapes from the galaxy and infrared emission is no longer proportional to SFR. Star formation rates can then be estimated from an uncorrected UV and an infrared

component ($SFR = SFR_{UV} + SFR_{IR}$). The infrared luminosity is then given by:

$$L_{IR} = \frac{SFR_{IR}}{K} = \frac{SFR}{K} \times \frac{10^{0.4 \times r_{UV}}}{1 + 10^{0.4 \times r_{UV}}} = \frac{SFR}{K} \times g(M_\star), \quad (10)$$

where r_{UV} is the ratio between obscured and unobscured star formation. We use the r_{UV} - M_\star relation of Pannella et al. (2009) to compute $g(M_\star)$:

$$r_{UV} = 2.5 \log \left(\frac{SFR_{IR}}{SFR_{UV}} \right) = 4.07 \times \log \left(\frac{M_\star}{M_\odot} \right) - 39.32. \quad (11)$$

$g(M_\star)$ tends to 0 at low mass and 1 at high mass. The UV light from young stars thus totally escapes the low-mass galaxies, but is fully reprocessed and emitted in as infrared radiation in massive galaxies. This is due to a larger amount of dust in massive galaxies, which causes a larger attenuation.

We used the same spectral energy distribution (SED) templates as B12, based on Magdis et al. (2012). There are different templates for main-sequence and starburst galaxies, both of which are assumed to evolve with redshift. We do not adopt a single template for a given type of galaxy at a given redshift, but assume a scatter on the mean interstellar radiation field $\langle U \rangle$, following B12. These SEDs were calibrated using $z < 2$ data, which show a rise of the (rest-frame) dust temperature with redshift. At higher redshift, we assume no evolution. This assumption will be discussed in Sect. 7. In this paper, we neglect the contribution of AGN, which is only significant in the mid-infrared (B12).

4. Computation of CIB power spectrum

We aim to compare the CIB anisotropies predicted by our model to observations in order to test its validity. This section presents the formalism used to derive the power-spectrum (cross-spectrum) of the CIB at a given waveband (between two wavebands, respectively). One of the key benefits of the relation we established between SFR and M_h is the fact that we can then rely on the well-known clustering properties of dark matter halos to predict the clustering of star-forming galaxies, and thus of CIB anisotropies. We use a method similar to Shang et al. (2012). However, we modified their formalism to obtain a more natural notation and avoid renormalization of all terms by the total emissivity of infrared galaxies at a given redshift.

4.1. Mean infrared emissivities of dark matter halos

One of the key ingredients to compute is the mean emissivities of the halos. Classical CIB models assume that clustering and emissivity are independent and compute the total emissivity of galaxies at a given redshift. This approximation is not exact and both emissivity and clustering vary with halo mass (see e.g. Béthermin et al. 2012b). We thus introduce the differential emissivity $dj_v/d\log(M_h)$ of dark matter halos as a function of halo mass. This differential emissivity is the sum of the contribution of central galaxy and satellite galaxies:

$$\frac{dj_v}{d\log(M_h)}(M_h, z) = \frac{dj_{v,c}}{d\log(M_h)}(M_h, z) + \frac{dj_{v,sub}}{d\log(M_h)}(M_h, z). \quad (12)$$

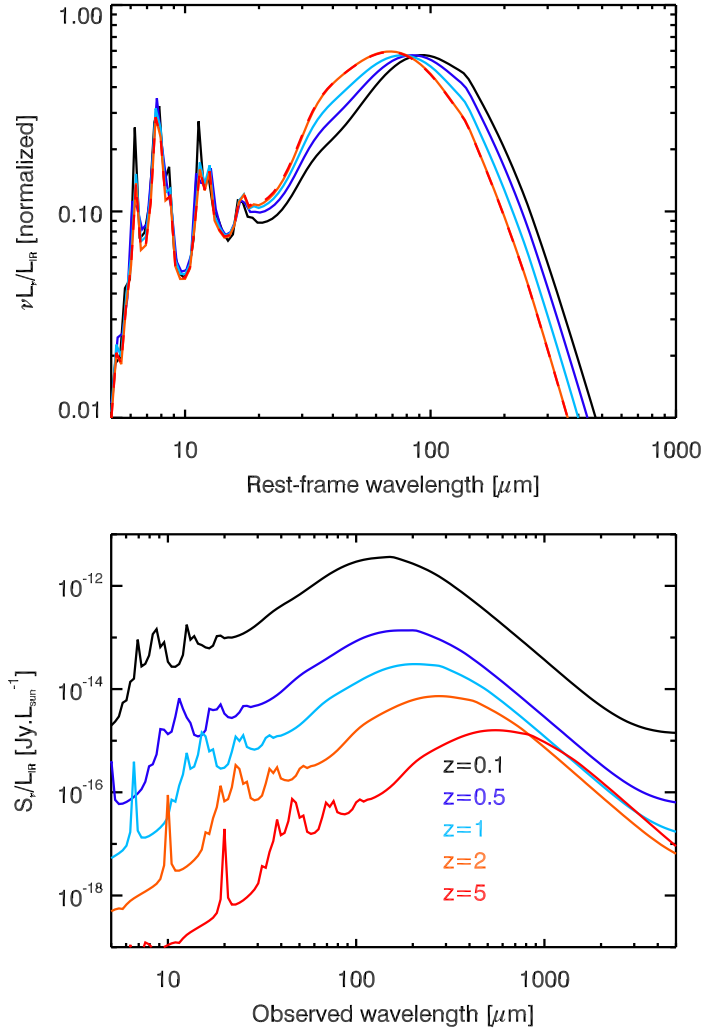


Fig. 3. Effective SEDs of infrared galaxies used in our model at various redshift. The upper panel shows the SEDs in νL_ν units normalized at $L_{IR} = 1 L_\odot$ as a function of rest-frame wavelength. The lower panel shows the ratio between the observed flux density and L_{IR} as a function of observed wavelength.

The contribution of central galaxies to the differential emissivity is computed from mean infrared flux of galaxies hosted by a halo of mass M_h and the HMF:

$$\begin{aligned} \frac{dj_{v,c}}{d\log(M_h)}(M_h, z) &= \frac{d^2 N}{d\log(M_h) dV} \times D_c^2 (1+z) \\ &\times \frac{SFR_{MS}(M_\star = f(M_h), z)}{K} \times g(M_\star = f(M_h), z) \\ &\times s_v^{\text{eff}}(z) \times (1 - q(M_\star = f(M_h), z)), \end{aligned} \quad (13)$$

where D_c is the comoving distance and $s_v^{\text{eff}}(z)$ is the effective SED of infrared galaxies at a given redshift, i.e. the mean flux density received from a population of star-forming galaxies with a mass corresponding to a mean infrared luminosity of $1 L_\odot$ (see Fig. 3), and $q(M_\star = f(M_h), z)$ is the fraction of quenched galaxies (i.e. non star-forming galaxies) as defined in Sect. 3.2. The shape of sSFR distribution being invariant with mass in our model, the mean flux density coming from a more massive population can thus be obtained just rescaling this SED taking into account the attenuation ($g(M_\star)$ defined in Eq. 10) and the SFR- M_\star relation. The effective SED is thus the mean of each type

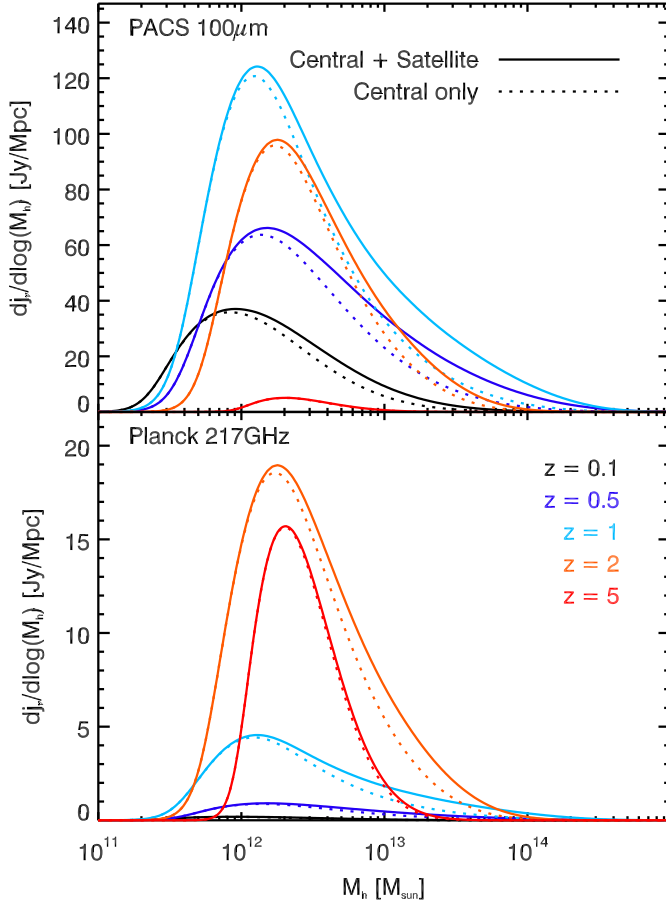


Fig. 4. Differential emissivities at $100\,\mu\text{m}$ (3000 GHz) and $1.38\,\text{mm}$ (217 GHz) as a function of halo mass at various redshift predicted by model C. The solid lines are the contributions of all the galaxies to the infrared flux of a main halo, when the dotted lines indicate only the contribution of central galaxies.

of SED weighted by their contributions to the background (provided by Eq. 7):

$$s_v^{\text{eff}}(z) = \int [p_{\text{MS}} \times \langle s_v^{\text{MS}} \rangle + p_{\text{SB}} \times \langle s_v^{\text{SB}} \rangle] ds\text{SFR}, \quad (14)$$

where

$$\langle s_v^{\text{MS or SB}} \rangle = \int p_{\text{MS or SB}}(\langle U \rangle | z) \times s_v^{\text{MS or SB}}(\langle U \rangle, z) \times d\langle U \rangle \quad (15)$$

with $\langle U \rangle$ is the intensity of the radiation field (strongly linked to dust temperature), $p(\langle U \rangle | z)$ its probability distribution (this encodes the information on the scatter of dust temperatures), and $s_v^{\text{MS or SB}}$ the flux density received from a $L_{\text{IR}} = 1 L_{\odot}$ main-sequence or starburst source with a radiation field $\langle U \rangle$ at redshift z . $\langle s_v^{\text{MS or SB}} \rangle$ is thus the average SED of a MS or SB galaxies at a given redshift taking into account the scatter on $\langle U \rangle$. Note that the infrared luminosity of these effective templates are slightly larger than $1 L_{\odot}$ because of the asymmetry of sSFR distribution caused by starburst. The effective SEDs from Eq. 14 used in this work are available online⁴.

The contribution of satellite galaxies to differential emissivity is the sum of the contribution of all galaxies in sub-halos of a main halo of mass M_h . It depends on the mass function of main

halos, the mass function of sub-halos in main halos of this mass, and the mean flux density of galaxies hosted by sub-halos:

$$\begin{aligned} \frac{dj_{v,\text{sub}}}{d\log(M_h)}(M_h, z) &= \frac{d^2N}{d\log(M_h)dV} \times D_c^2(1+z) \\ &\times \int s_v^{\text{eff}}(z) \frac{dN}{d\log(m_{\text{sub}})}(m_{\text{sub}}|M_h) \times \frac{\text{SFR}_{\text{MS}}(M_{\star} = f(m_{\text{sub}}), z)}{K} \\ &\times g(M_{\star} = f(m_{\text{sub}}), z) \times (1 - q(M_{\star} = f(m_{\text{sub}}), z)) d\log(m_{\text{sub}}). \end{aligned} \quad (16)$$

In this formula, we assume that the quenching of satellite galaxies depends only on their stellar mass (or sub-halo mass). We also propose an alternative scenario, where quenching depends on the mass of the main halo and not on the mass of the sub-halo. In this scenario, satellite galaxies become quenched at the same time as the central galaxy in the same parent halo. In practice, we replace m_{sub} by M_h in the last factor of Eq. 16, which can then be moved outside the integral. This scenario is motivated by the fact that the fraction of quenched satellite galaxies tends to be higher in dense environments (e.g. Park et al. 2007). This phenomenon is often called environmental quenching. The modified version of model B where this modification was performed is called model C.

In our computation, the flux densities are not the monochromatic flux densities at the center of the passband filters of each instrument, but are computed taking into account the real filter profiles. Fig. 4 illustrates the variation of differential emissivities with halo mass, redshift and wavelength. Due to the shape of the SEDs, long wavelengths have stronger emissivities at high redshift. Note that the halo mass dominating the emissivities is always $\sim 10^{12} M_{\odot}$ in agreement with previous works (e.g. Conroy & Wechsler 2009; Béthermin et al. 2012b; Wang et al. 2012; Behroozi et al. 2012a).

4.2. Power spectrum

The CIB power spectrum is the sum of three contributions (Amblard & Cooray 2007; Viero et al. 2009; Planck Collaboration et al. 2011; Amblard et al. 2011; Pénin et al. 2012a; Shang et al. 2012):

- 2-halo term: correlated anisotropies between galaxies in different halos, which dominates at scales larger than a few arcminutes.
- 1-halo term: correlated anisotropies of galaxies inside the same main halo, which have a significant impact at scales of a few arcminutes.
- Poisson term: non correlated Poisson anisotropies, also called shot noise, which dominate at small scales.

The cross power spectrum of CIB $C_{\ell, \nu\nu'}$ between two frequency bands (ν and ν') is thus:

$$C_{\ell, \nu\nu'} = C_{\ell, \nu\nu'}^{2h} + C_{\ell, \nu\nu'}^{1h} + C_{\ell, \nu\nu'}^{\text{poi}} \quad (17)$$

The 2-halo and 1-halo terms, which correspond to large and intermediate scale anisotropies respectively, are computed from the mean emissivities of galaxies and are not affected by the stochasticity of the connexions between galaxies and halos. The anisotropies caused by the scatter of galaxy properties are

⁴ <http://irfu.cea.fr/Sap/Phoceia/Page/index.php?id=537>

described by the Poisson term, which requires no assumption regarding the link between dark matter halos and galaxies and is deduced only from the B12 model. Each term is calculated independently, but based on the same consistent model.

4.2.1. 2-halo term

The 2-halo term is computed from the following formula, summing on redshift, but also over all cross-correlation between halos of various mass:

$$C_{\ell, \nu\nu'}^{2h} = \iiint \frac{dD_c}{dz} \left(\frac{a}{D_c} \right)^2 \left(\frac{dj_{\nu,c}}{d\log(M_h)}(z) + \frac{dj_{\nu,\text{sub}}}{d\log(M_h)}(z)u(k, M_h, z) \right) \times \left(\frac{dj_{\nu',c}}{d\log(M_h')}(z) + \frac{dj_{\nu',\text{sub}}}{d\log(M_h')}(z)u(k, M_h', z) \right) b(M_h, z)b(M_h', z) \times P_{\text{lin}}(k = \frac{l}{D_c}, z) d\log M_h d\log M_h' dz. \quad (18)$$

The first factor is geometrical. The next two factors contain differential emissivities. $u(k, M_h, z)$ is the Fourier transform of the halo profile assumed here to be NFW (Navarro et al. 1997). In contrast with Shang et al. (2012), this term is placed only in front the sub-halo-emissivity term, assuming that sub-halos are distributed following the NFW profile. The central galaxy is assumed to be at the center of the halo. The clustering term ($b(M_h)b(M_h')P_{\text{lin}}$) is the cross power-spectrum between halo of mass M_h and M_h' , under the assumption that $P(k, M_h, M_h') = b(M_h)b(M_h')P_{\text{lin}}$ (Cooray & Sheth 2002). Eq. 18 can be significantly simplified introducing:

$$J_\nu(z, k) = \int b(M, z) \left(\frac{dj_{\nu,c}}{d\log(M_h)} + \frac{dj_{\nu,\text{sub}}}{d\log(M_h)}u(k, M_h, z) \right) dM_h, \quad (19)$$

which is an emissivity weighted by the bias corresponding to each halo mass. We can then simplify Eq. 18:

$$C_{\ell, \nu\nu'}^{2h} = \int \frac{dD_c}{dz} \left(\frac{a}{D_c} \right)^2 J_\nu(z, k) J_{\nu'}(z, k) P_{\text{lin}}(k = \frac{l}{D_c}, z) dz \quad (20)$$

This way of computing $C_{\ell, \nu\nu'}^{2h}$ reduces the number of integrals, because J_ν can be calculated only once per frequency channel and then can be used to derive all the cross-spectra. In addition, J_ν can also be used to compute the cross-correlation between CIB and CMB lensing (see Sect. 4.3).

4.2.2. 1-halo term

The 1-halo term is computed with:

$$C_{\ell, \nu\nu'}^{1h} = \iint \frac{dD_c}{dz} \left(\frac{a}{D_c} \right)^2 \times \left[\frac{dj_{\nu,c}}{d\log(M_h)} \frac{dj_{\nu',\text{sub}}}{d\log(M_h)} u(k, M_h, z) + \frac{dj_{\nu,\text{sub}}}{d\log(M_h)} \frac{dj_{\nu',c}}{d\log(M_h)} u(k, M_h, z) + \frac{dj_{\nu,\text{sub}}}{d\log(M_h)} \frac{dj_{\nu',\text{sub}}}{d\log(M_h)} u^2(k, M_h, z) \right] \times \left(\frac{d^2 N}{d\log(M_h) dV} \right)^{-1} dz d\log M_h \quad (21)$$

The first factor describes geometry. The second one represents the various (cross-)correlations between satellite and central galaxies. There is only a factor u for (cross-)correlation between satellites and central, because the central is assumed to be at the center of the halo and the satellites follow the NFW profile, and u^2 for satellite-satellite combinations. Finally, we have to renormalize by the inverse of the mass function, because the two $dj/d\log(M_h)$ factors contain implicitly two times the number of halos, when this should appear only once (Cooray & Sheth 2002). This notation avoid to have to renormalize by j_ν as in Shang et al. (2012).

4.2.3. Poisson term

The Poisson term is independent of large-scale halo and only depends on the flux distribution of galaxies (number counts). These Poisson anisotropies for the auto power spectrum can be computed from (Lagache et al. 2003):

$$C_{\ell, \nu\nu}^{\text{poi}} = \int_0^{S_{\nu, \text{cut}}} S_\nu^2 \frac{dN}{dS_\nu} dS_\nu. \quad (22)$$

Here dN/dS_ν are the differential number counts (see e.g. B12 for the computational details) and $S_{\nu, \text{cut}}$ is the flux cut at which sources are removed from the maps. The Poisson term of the cross-spectrum is slightly more complex to compute:

$$C_{\ell, \nu\nu'}^{\text{poi}} = \int_0^{S_{\nu, \text{cut}}} \int_0^{S_{\nu', \text{cut}}} S_\nu S_{\nu'} \frac{d^2 N}{dS_\nu dS_{\nu'}} dS_\nu dS_{\nu'}, \quad (23)$$

where $d^2 N/dS_\nu dS_{\nu'}$ are the multivariate counts (i.e. number of sources with a flux between S_ν and $S_\nu + dS_\nu$ in one band and $S_{\nu'}$ and $S_{\nu'} + dS_{\nu'}$ in the other).

In practice, multivariate counts are hard to compute, and summing the contribution of various redshift, type of galaxies, infrared luminosity, and radiation field is easier (the derivation of this formula is presented in Appendix B):

$$C_{\ell, \nu\nu'}^{\text{poi}} = \int_z \frac{dV}{dz} \sum_{\{\text{MS, SB}\}} \int_{\langle U \rangle} P_{\text{MS or SB}}(\langle U \rangle | z) \int_{L_{\text{IR}}=0}^{L_{\text{IR, cut}}^{\text{MS or SB}}(\langle U \rangle, z)} \frac{d^2 N_{\text{MS or SB}}}{dL_{\text{IR}} dV} L_{\text{IR}}^2 s_{\nu}^{\text{MS or SB}}(\langle U \rangle, z) \times s_{\nu'}^{\text{MS or SB}}(\langle U \rangle, z) dL_{\text{IR}} d\langle U \rangle dz \quad (24)$$

where $L_{\text{IR, cut}}^{\text{MS or SB}}(\langle U \rangle, z)$ is the infrared luminosity where the source is detected in at least one of the bands (depends on redshift, type of galaxy and radiation field), $d^2 N_{\text{MS or SB}}/dL_{\text{IR}} dV$ is the infrared luminosity function (main-sequence or starburst contribution).

4.3. Cross-correlation between CIB and CMB lensing

In addition to cross-correlations between the CIB in various bands, we can also test the predictive power of our model for correlation between the CIB and the reconstructed gravitational potential derived from distortions of the CMB due to gravitational lensing by large scale halos at $z \sim 1-3$ (e.g. Hanson et al. 2009). This correlation is a direct probe of the link between the gravitational potential of dark matter halos and infrared emission from star-forming galaxies.

Because the CMB lensing signal is due to dark matter halo, this signal can be modeled with a 2-halo term replacing the term of emissivity by a term linked to the gravitational potential (adapted from Planck Collaboration et al. 2013):

$$C_{\ell,\phi\nu} = \int \frac{dD_c}{dz} \left(\frac{a}{D_c} \right) J_\nu(z, \ell) \Phi(z, k) P_{\text{lin}}(k = \frac{l}{D_c}, z) dz, \quad (25)$$

$\Phi(z, \ell)$ is given by (Challinor & Lewis 2005), :

$$\Phi(z, \ell) = \frac{3}{l^2} \Omega_M \left(\frac{H_0}{c} \right)^2 \frac{D_c}{a} \frac{D_c^{\text{CMB}} - D_c(z)}{D_c^{\text{CMB}} \times D_c(z)}, \quad (26)$$

where H_0 is the Hubble constant, Ω_M the matter density in units of the critical density, and D_c^{CMB} the comoving distance between CMB and us. The impact of sub-halos on CMB lensing (1-halo) is quite small and can be neglected for this work.

5. Computation of angular correlation function of resolved infrared galaxies

In addition to the anisotropies of the faint infrared sources responsible for the unresolved background, our model also provides predictions of the angular correlations of the individually detected bright sources. A formalism taking into account the selection function of the resolved sources has to be employed and we thus cannot use the same formalism as for the power-spectrum. In this paper, we only consider samples selected using a flux threshold ($S_{\nu, \text{cut}}$) at a given wavelength for simplicity. In this section, we first explain how we compute the halo occupation distribution (HOD, i.e. the mean number of central and satellite galaxies as a function of halo mass and redshift) for a given selection of resolved sources and then how we derive the correlation function from the HODs.

5.1. Halo occupation distribution

The mean number of central galaxies in a given halo of total mass M_h is:

$$\langle N_c \rangle(M_h, z) = (1 - q(M_\star = f(M_h), z)) \times \sum_{\text{type}} \int_{\text{sSFR}} \int_{\langle U \rangle} H(s_{\nu}^{\text{MS or SB}}(\langle U \rangle, z) \times L_{\text{IR}}(M_\star = f(M_h), \text{sSFR}) > S_{\nu, \text{cut}}) d\langle U \rangle ds\text{SFR}, \quad (27)$$

where $q(M_\star = f(M_h), z)$ is the fraction of quenched objects and H is a function having a value of 1 if the condition is true and 0 otherwise. This condition is true only if the source is sufficiently bright to be detected ($S_\nu > S_{\nu, \text{cut}}$). This depends on both halo mass, type of galaxy (MS or SB), sSFR, and $\langle U \rangle$.

The number of satellites depends on the total mass of the parent halo M_h and is connected to sub-halo via:

$$\langle N_{\text{sub}} \rangle(M_h, z) = \int_{m_{\text{sub}}} \frac{dN}{d\log(m_{\text{sub}})} (m_{\text{sub}} | M_h) \langle N_c \rangle(m_{\text{sub}}, z) dm_{\text{sub}}. \quad (28)$$

This formula is true only when we assume the same infrared luminosity versus halo mass relation for main and sub-halos (model A and B) and consequently the HOD of the satellite in a given sub-halo of mass m_{sub} is the same as

for the central in a main halo of identical mass $M_h = m_{\text{sub}}$. For model C (satellites quenched at the same time as the centrals), the factor $\langle N_c \rangle(m_{\text{sub}}, z)$ has to be multiplied by $(1 - q(M_\star = f(M_h), z)) / (1 - q(M_\star = f(m_{\text{sub}}), z))$ to take into account the fact that in this version of the model the quenching is linked to the mass of the central and not the satellite.

Fig. 5 shows the HOD of $S_{160} > 5 \text{ mJy}$ (sources detected by the deepest PACS surveys) and $S_{850} > 3 \text{ mJy}$ (typical sub-millimeter galaxies) sources at low ($z=0.1$) and high ($z=2$) redshift. The number of central galaxies decreases very quickly at low mass. This sharp cut is due to the selection in infrared flux and the rather tight correlation between infrared luminosity and halo mass for central galaxies. At low redshift, the probability to detect an infrared galaxy in a massive halo is pretty small because the vast majority of central galaxies are quenched and thus have little infrared emission. The HOD of satellite strongly depends on the version of the model. If the quenching of satellites is decorrelated from the quenching of the centrals (model A and B), the number of detected satellite increases quickly with the halo mass. This is not the case for model C, for which the satellites are quenched at the same time as the centrals.

5.2. Angular auto-correlation function

The angular correlation function (ACF) can be compute from the HOD of galaxies and their redshift distribution (see Cooray & Sheth 2002 for a review):

$$w(\theta) = \frac{\int_z \left(\frac{dN}{dz} \right)^2 \int_k \frac{k}{2\pi} P_{\text{gg}}(k, z) J_0(k D_c \theta) dz}{\left(\int_z \frac{dN}{dz} dk dz \right)^2}, \quad (29)$$

where J_0 is the zero-th order Bessel function and dN/dz the redshift distribution of galaxies, which can be computed from counts per redshift slice following Béthermin et al. (2011). P_{gg} is the sum of two terms corresponding to the clustering of galaxies in two different halos and inside the same halo:

$$P_{\text{gg}}(k, z) = P_{\text{gg}}^{2\text{h}}(k, z) + P_{\text{gg}}^{1\text{h}}(k, z). \quad (30)$$

Following the standard conventions, we write the 2-halo term as:

$$P_{\text{gg}}^{2\text{h}}(k, z) = \left[\int_{M_h} \frac{d^2 N}{d\log(M_h) dV} b(M_h) \frac{\langle N_{\text{gal}} \rangle}{\bar{n}_{\text{gal}}} dM_h \right]^2 P_{\text{lin}}(k, z), \quad (31)$$

where $\langle N_{\text{gal}} \rangle = \langle N_c \rangle + \langle N_{\text{sub}} \rangle$. The 1-halo term is:

$$P_{\text{gg}}^{1\text{h}}(k, z) = \int_{M_h} \frac{d^2 N}{d\log(M_h) dV} \frac{2\langle N_c \rangle \langle N_{\text{sub}} \rangle + \langle N_{\text{sub}} \rangle^2 u^2(k, M_h, z)}{\bar{n}_{\text{gal}}} dM_h, \quad (32)$$

where

$$\bar{n}_{\text{gal}} = \int \frac{d^2 N}{d\log(M_h) dV} \langle N_{\text{gal}} \rangle dM_h. \quad (33)$$

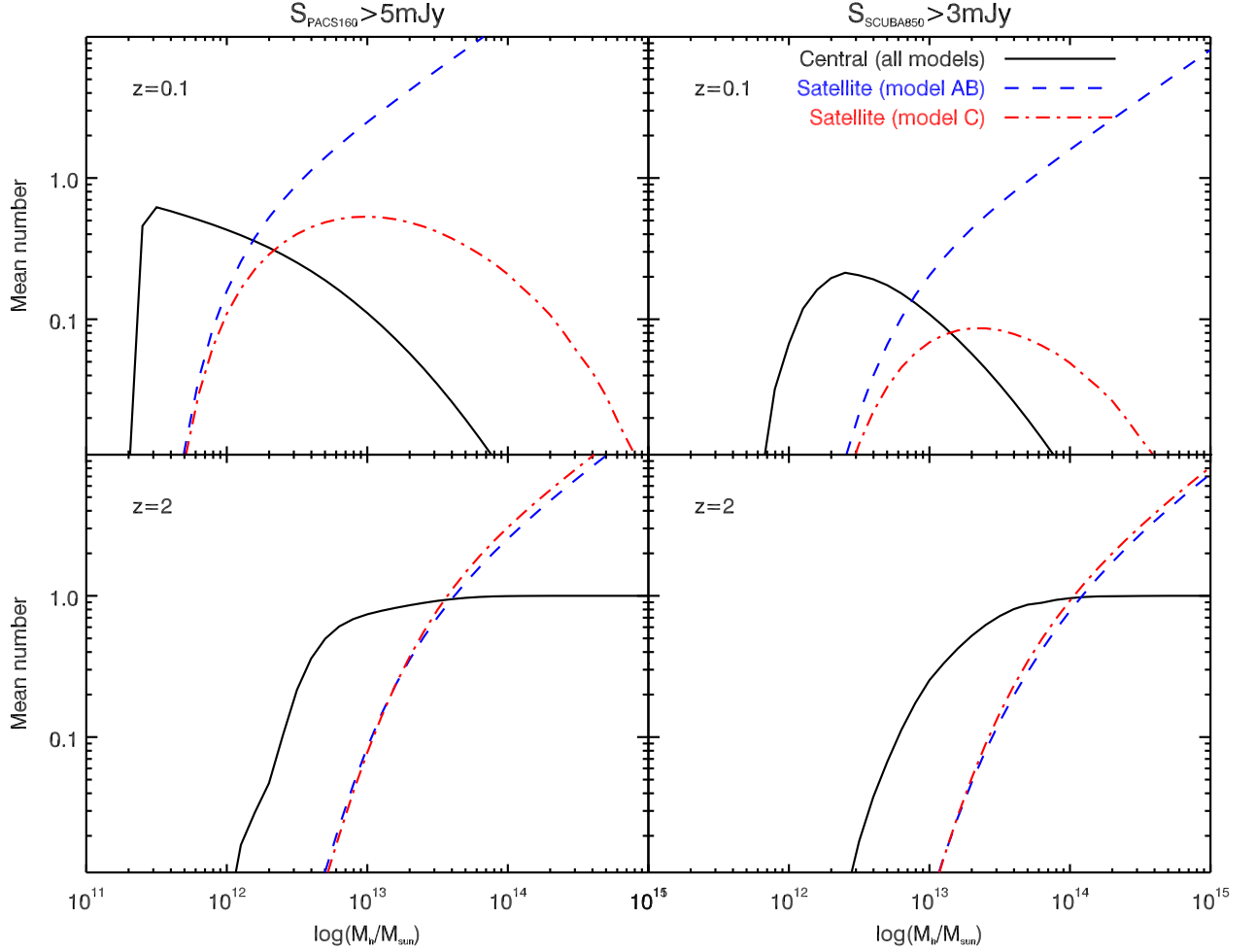


Fig. 5. Halo occupation distribution, i.e. mean number of detected galaxies in a halo, including its sub-structures, as a function of its total mass M_h , of $S_{160} > 5 \text{ mJy}$ (left) and $S_{850} > 3 \text{ mJy}$ (right) sources at $z = 0.1$ (top) and $z=2$ (bottom) for central (solid line) and satellite (dashed line) galaxies predicted by the model. The HOD of central galaxies is the same for all the version of the models and represented in black. Satellite HODs are plotted in blue (red, respectively) for model A/B (C, respectively).

6. Comparison with the observations

6.1. CIB power spectrum and number counts

We compared the predictions of our model with the CIB power-spectrum measured with IRAS ($100 \mu\text{m}$, Pénin et al. 2012b), *Spitzer* ($160 \mu\text{m}$, Lagache et al. 2007 and Pénin et al. 2012b), *Herschel* (250 , 350 , and $500 \mu\text{m}$, Viero et al. 2012), *Planck* (350 , 550 , 850 , and $1380 \mu\text{m}$, Planck Collaboration et al. (2011)), and SPT ($1380 \mu\text{m}$, Hall et al. 2010) measurements in Fig. 6 (left and center). The level of the Poisson anisotropies is significantly affected by the flux cut used to mask bright sources, and their level increases with the chosen flux cut. The correlated anisotropies (1-halo and 2-halo) are less affected by the flux cut. When we compare several datasets at the same wavelength, we thus compute the model predictions for the flux cut of the experiment which is the most sensitive at small scales. The flux cuts used to compute the model predictions are thus 1 Jy at $100 \mu\text{m}$, 100 mJy at $160 \mu\text{m}$, 0.3 mJy at $250 \mu\text{m}$, $350 \mu\text{m}$, and $500 \mu\text{m}$, 0.54 Jy at $550 \mu\text{m}$ (545 GHz), 0.325 Jy at $850 \mu\text{m}$ (353 GHz), 20 mJy at 1.38 mm (217 GHz). The overall agreement with the data is very good for a model not fitted on the data. However, some tensions between model A and B and data at short and large wavelengths provide interesting

information.

The anisotropies at $100 \mu\text{m}$ are dominated by galaxies at low redshift (see Sect. 8) and are thus not affected by the evolution of galaxies at $z > 2.5$. Consequently, there is no difference between model A and B. On the contrary, model C (with quenching of satellite around massive quenched central) predicts a lower level of anisotropies at $\ell < 5000$, which is in better agreement with the data, especially around $\ell = 2000$. The "environmental quenching" in model C reduces strongly the 1-halo term compared to model B (by a factor of 4 at $\ell=2000$), but does not significantly affect the 2-halo term ($\sim 15\%$) and does not change the Poisson level at all. However, the former difference is not very significant ($\sim 2\sigma$) and CIB anisotropies are obviously not the best probe of such environmental effects.

The interpretation of *Spitzer*/MIPS $160 \mu\text{m}$ data is more tricky. While the measurements of Lagache et al. (2007) (crosses) agree with our data, measurements of Pénin et al. (2012b) (asterisks) are a factor 3-10 higher than our model at large scales ($\ell < 2000$). Such a large difference is unexpected, especially when we consider that the model agrees well with the data at 100 and $250 \mu\text{m}$. However, MIPS suffers from strong $1/f$ noise and is not the best instrument to measure large scale

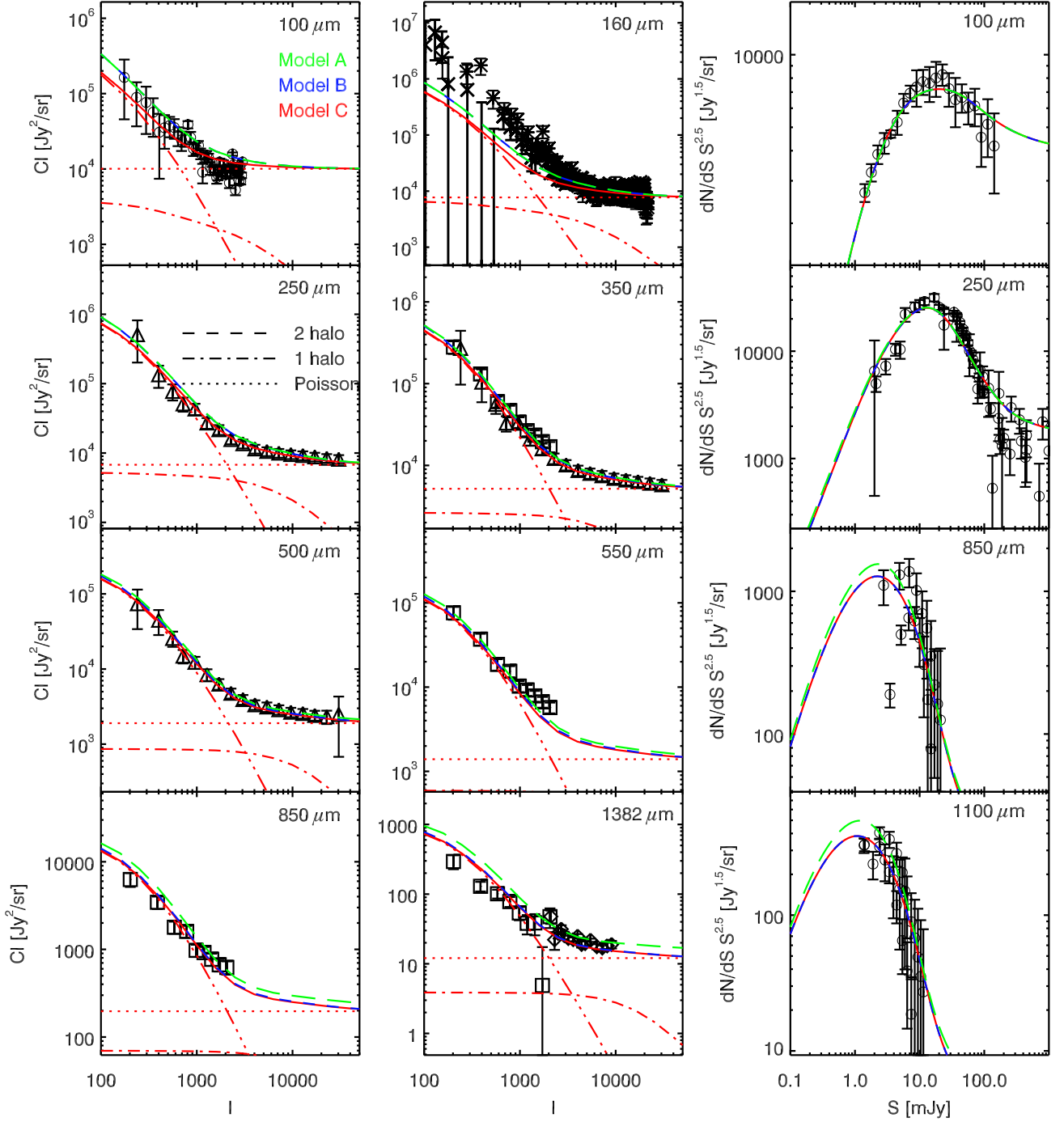


Fig. 6. *Left and center panels:* CIB power spectrum predicted by our model and comparison with IRAS (100 μm , Pénin et al. 2012b, *open circles*), *Spitzer* (100 μm , Lagache et al. 2007, *crosses*, Pénin et al. 2012b, *asterisks*), *Herschel* (250, 350, and 500 μm , Viero et al. 2012, *triangles*), *Planck* (350, 550, 850, and 1380 μm , Planck Collaboration et al. (2011), *squares*), and SPT (1380 μm , Hall et al. 2010, *diamonds*) measurements. The dotted, dot-dashed, and dotted lines represent the Poisson, 1-halo, and 2-halo terms. *Right panel:* Number counts of infrared galaxies. Data are taken from the compilation of measurements in Béthermin et al. (2011) and B12. Model A, B, and C are represented with a green long-dash, a blue short-dash, a red solid line, respectively.

anisotropies.

Between 250 and 550 μm , our model nicely agrees with *Planck* and *Herschel* measurements. At longer wavelengths (850 μm and 1.4 mm), model A over-predicts anisotropies at

large scale by a factor 2 at 1.4 mm, while models B and C agree with the data, except for a 2σ tension at 1.4 mm in the two lowest-multipole bins. However, measuring the CIB at 217 GHz is difficult because it strongly relies on the correct subtraction of the CMB. Future analyses will either confirm

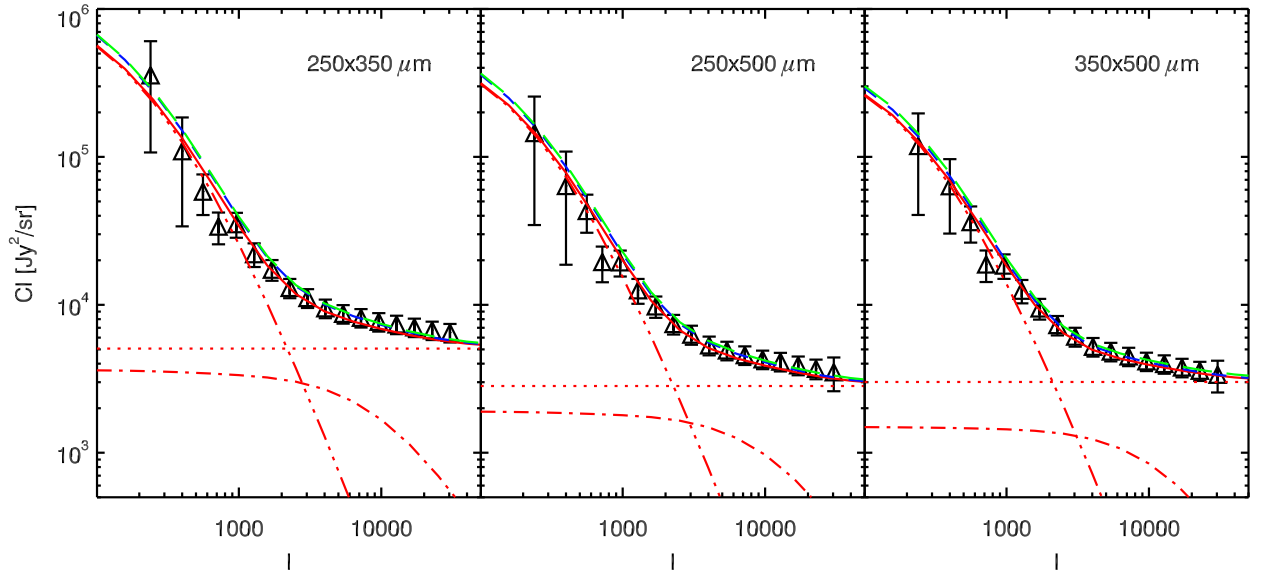


Fig. 7. Cross-power spectrum between SPIRE bands measured by Viero et al. (2012) and comparison with our model. Model A, B, and C are represented with a green long-dash, a blue short-dash, a red solid line, respectively.

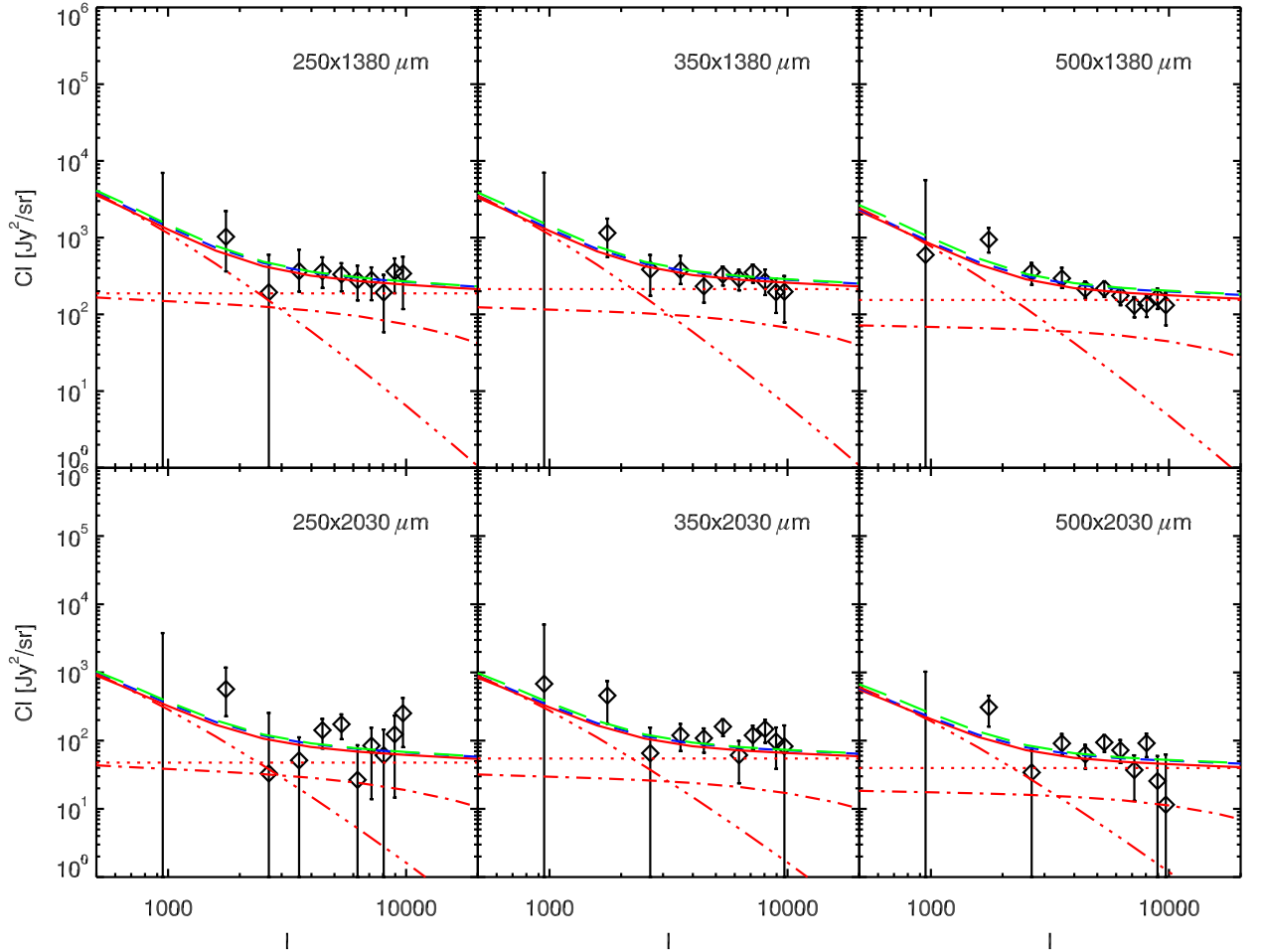


Fig. 8. Cross-power spectrum between BLAST and ACT measured by Hajian et al. (2011) and comparison with our model. Model A, B, and C are represented with a green long-dash, a blue short-dash, a red solid line, respectively.

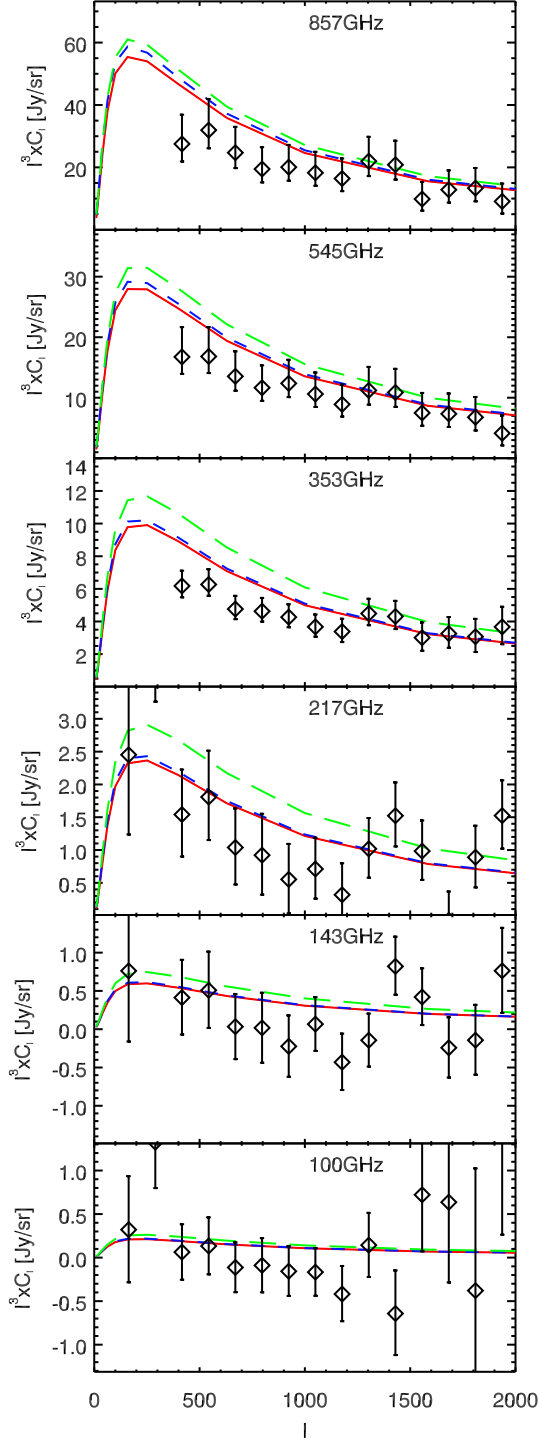


Fig. 9. Cross-power-spectrum between CIB and CMB lensing measured by Planck Collaboration et al. (2013) and comparison with our model. Model A, B, and C are represented with a green long-dash, a blue short-dash, a red solid line, respectively.

or refute the presence of this discrepancy. The three models agree with the number counts at $850\mu\text{m}$ and 1.1 mm . The difference between model A and B/C is the sSFR at $z > 2.5$ and the characteristic density of the mass function of star-forming galaxies. Model A assumes a flat sSFR at $z > 2.5$, while models B and C assume rising sSFR at $z > 2.5$ compensated by a decrease of the characteristic density of the mass function to preserve the

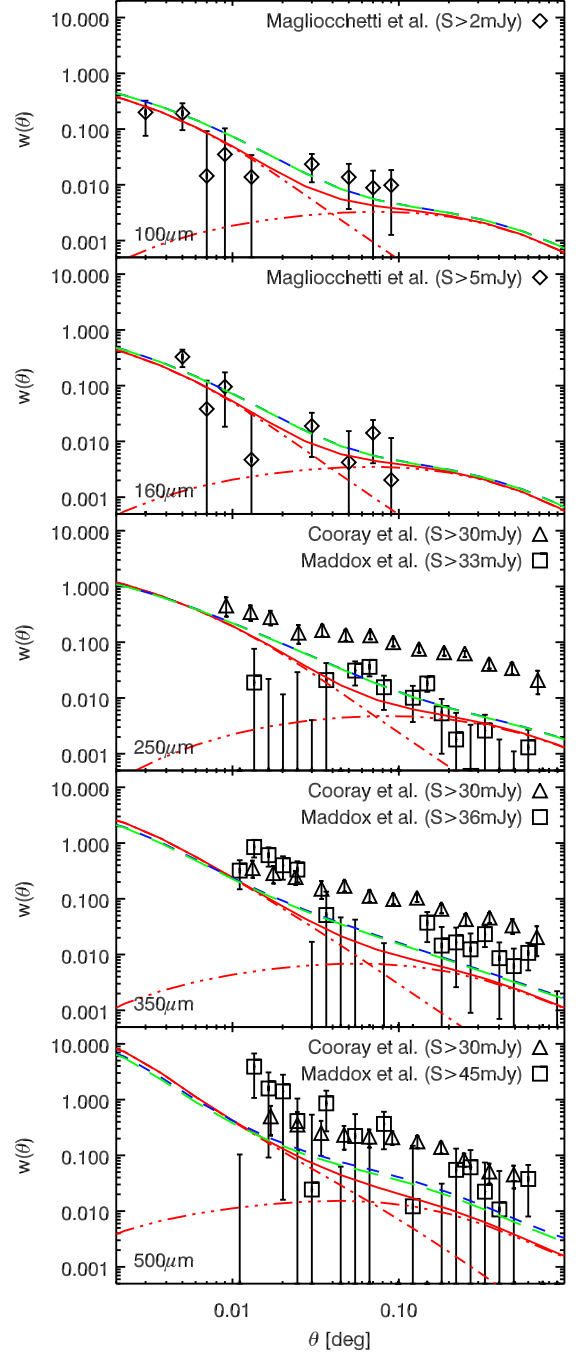


Fig. 10. Auto-correlation function of various flux-selected sample of infrared galaxies and comparison with our model (same color coding as in Fig. 6). The data come from Magliocchetti et al. (2011) at $100\mu\text{m}$ and $160\mu\text{m}$ and Cooray et al. (2010) and Maddox et al. (2010) at 250 , 350 , and $500\mu\text{m}$. We used the same flux cuts as Magliocchetti et al. (2011) and Cooray et al. (2010). Model A, B, and C are represented with a green long-dash, a blue short-dash, a red solid line, respectively.

agreement with the number counts. In these two versions, the number of bright objects is thus the same, but the number of faint objects is different (see e.g. number counts around 1 mJy at 1.1 mm). Model A over-predicts the CIB anisotropies because of a too high emissivity of high-redshift faint galaxies.

In the case of the model C (which includes satellite-quenching), the 1-halo term never dominates the anisotropies

regardless of wavelength or scale. Concerning models A and B (without satellite-quenching), the 1-halo term contributes to the CIB anisotropies by a similar amount as do the 2-halo and Poisson terms at $\ell \sim 2000$ at $100\mu\text{m}$, $160\mu\text{m}$, and $250\mu\text{m}$. At other scales and wavelengths, it represents a minor contribution. This result is in contradiction with models assuming no mass-luminosity dependence (e.g. Planck Collaboration et al. 2011; Pénin et al. 2012a), but consistent with the approaches assuming a dependence (e.g. Shang et al. 2012). This reduction of the 1-halo term is caused by the fact that satellites are hosted by low mass sub-halos and thus have low infrared luminosities.

6.2. CIB cross-power-spectrum

In addition to auto power spectra, we can compare the predictions of our model with cross power spectra. These cross-power spectra are useful to verify if the level of correlation between bands is correct. This also is an indirect test of whether SED libraries and redshift distributions used in the model are correct. We have compared our models with measurements of Viero et al. (2012) between SPIRE bands (see Fig. 7). All versions of our model agree with the data, except a systematic 2σ tension for the point at $\ell = 700$ in the three bands which could be due to cosmic variance (note that one 2σ outlier for 18 points is statistically expected). The trends of Hajian et al. (2011) (see Fig. 8) are also well reproduced, but our model is systematically lower than the data at $\ell = 1500$. However, the stability of BLAST at large scales is not as good as for SPIRE. A future analysis of the cross-correlation between SPIRE and ACT and/or between *Planck* bands will thus be useful to further investigate this discrepancy.

6.3. Cross correlation between CIB and CMB lensing

In Fig. 9, we compare the predictions of the cross-correlation between CIB and CMB lensing with the measurements from Planck Collaboration et al. (2013). At $\ell > 1000$, all versions of the model agree well with the data. At $\ell < 1000$, the various versions of the model tends to be systematically higher than the data. Models B and C (with modified evolution at high redshift) are closer from the data, but over-predict the cross-correlation by 1σ at 857 GHz and 545 GHz and 2σ at 353 GHz. Future works will investigate this tension.

6.4. Clustering of resolved galaxies

The clustering of bright resolved infrared sources is also an important test of our model. Fig. 10 shows the comparison between the clustering measurements of various flux-selected samples and our model predictions. At 100 and $160\mu\text{m}$, our model agrees well with the *Herschel*/PACS measurements of Magliocchetti et al. (2011). In *Herschel*/SPIRE bands, the comparison is more tricky. There are strong disagreements between the measurements of Cooray et al. (2010) and Maddox et al. (2010). In fact, measuring the correlation function of SPIRE sources (250 , 350 , and $500\mu\text{m}$) is very difficult because these data are strongly confusion-limited (Nguyen et al. 2010). The background is thus hard to estimate and the completeness of the catalog can vary depending on the local source density. We agree with Maddox et al. (2010) at scales larger than 0.1 deg , but not

at smaller scales at $250\mu\text{m}$ and $350\mu\text{m}$, where systematics could be due to background subtraction. Our model disagrees with the measurements of Cooray et al. (2010), which are systematically higher. More reliable measurements of the correlation function of SPIRE sources, controlling the systematic effects, are thus necessary to check accurately the validity of our model.

7. Successes and limitations of our model

In the previous sections, we presented a natural way of extending the B12 model of infrared galaxies by linking their properties to their host halo. We tested the validity of this approach comparing the prediction of this extended model to the measured spatial distribution of both individually-detected infrared galaxies (where the measurements are reliable) and the unresolved background. This comparison shows the good predictive power of our approach, suggesting that our assumptions are fair. Using this model to interpret both the origin of CIB anisotropies (Sect. 8) and the link between star-forming galaxies and dark matter halos (Sect. 9.3) is thus legitimate. For simplicity, we will perform this analyses only with model C, which provides the best agreement with the data.

However, some limitations of this model have to be kept in mind. Firstly, the SED of infrared galaxies at high redshift ($z > 2$) was not measured and it is not clear if the dust temperature will increase or decrease at high redshift, because of the uncertainties on the mass-metallicity and mass-attenuation relation as discussed in Magdis et al. (2012). The good agreement between the model and the CIB anisotropies at long wavelengths suggests that our hypothesis of non-evolution is reasonable. The SED of low mass galaxies ($M_\star < 10^{10} M_\odot$) is not well constrained, but the contribution of these low mass galaxies to the CIB is small and this scenario is thus hard to test. In addition, the specific star formation rate and the SMF of star-forming galaxies at very high redshift ($z > 3$) are also uncertain, but the effects of $z > 3$ galaxies on the CIB are pretty small and these data thus cannot accurately constrain the evolution of infrared galaxies at very high redshift. Finally, we assumed an universal relation between stellar mass and UV attenuation, but this relation could also break at very high redshift, where the amount of metals is smaller and galaxies could thus contain less dust. For all these reasons, the predictions of the models at $z > 2$ must be interpreted with caution.

8. Where do the CIB and its anisotropies come from?

In this section, we discuss the predictions of the model concerning the redshift distribution of the various signals we studied (CIB auto-spectra, CIB cross-spectra, CIBx CMB lensing). We base our analysis on the model C as motivated in Sect. 7.

8.1. Redshift distribution of CIB mean level and anisotropies

The CIB SED can be predicted directly from the Béthermin et al. (2012a) counts model. Fig. 11 (left upper panel) shows the spectral energy distribution of the CIB and its decomposition per redshift slice. Compared to Béthermin et al. (2011) model, this new model has a slightly higher contribution of $1 < z < 2$ sources. This new model agrees well with both absolute measurements and the total contribution of infrared galaxies

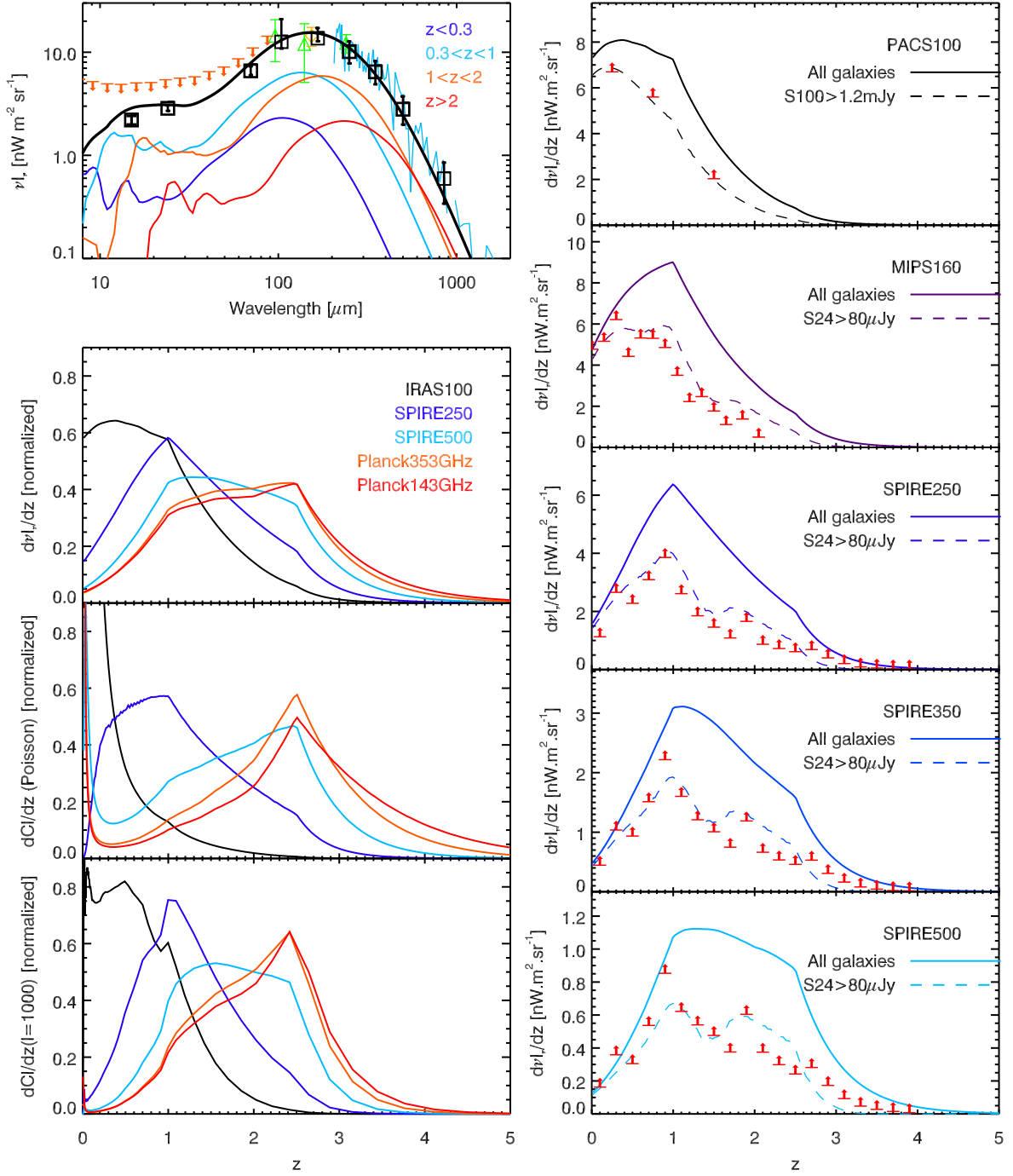


Fig. 11. Predicted redshift distribution of the CIB and its anisotropies. *Upper left panel:* CIB SED and contribution per redshift slice (colored solid lines). *black squares:* total extrapolated CIB from deep number counts (Teplitz et al. 2011; Béthermin et al. 2010a; Berta et al. 2011; Béthermin et al. 2012c; Zemcov et al. 2010). *Cyan solid line:* Absolute CIB spectrum measured by COBE/FIRAS (Lagache et al. 2000). *Green triangles:* absolute CIB measurements performed by COBE/DIRBE at $100\mu\text{m}$, $140\mu\text{m}$, and $240\mu\text{m}$ (updated in Dole et al. 2006). *Yellow diamond:* absolute measurements of Pénin et al. (2012a) at $160\mu\text{m}$ with Spitzer/MIPS. *Orange arrows:* upper limits derived from opacity of the Universe to TeV photons (Mazin & Raue 2007). *Lower left panel:* Normalized redshift distribution of the mean level (up), Poisson anisotropies (middle), large scale anisotropies at $\ell=1000$ (bottom). Various colors correspond to various bands. *Right panel:* Contribution of various redshifts to the CIB (solid line) and comparison with lower limits derived by stacking from Berta et al. (2011) at $100\mu\text{m}$, Jauzac et al. (2011) at $160\mu\text{m}$ and Béthermin et al. (2012c) at $250\mu\text{m}$, $350\mu\text{m}$, and $500\mu\text{m}$ (arrows). The dashed lines are the model predictions taking into account the selection used to derive the lower limits.

extrapolated from the number counts.

The three lower left panels of Fig. 11 show the redshift distribution of the intensity of the CIB (top), but also of its anisotropies at small (middle) and large scales (bottom). In order

to allow an easier comparison between bands, we normalized the redshift distributions in order to have $\int d(\nu I_\nu)/dz dz = 1$ and $\int dC_\ell/dz dz = 1$. Between $100\mu\text{m}$ (3000 GHz) and $850\mu\text{m}$ (353 GHz), the redshift distribution evolves strongly toward

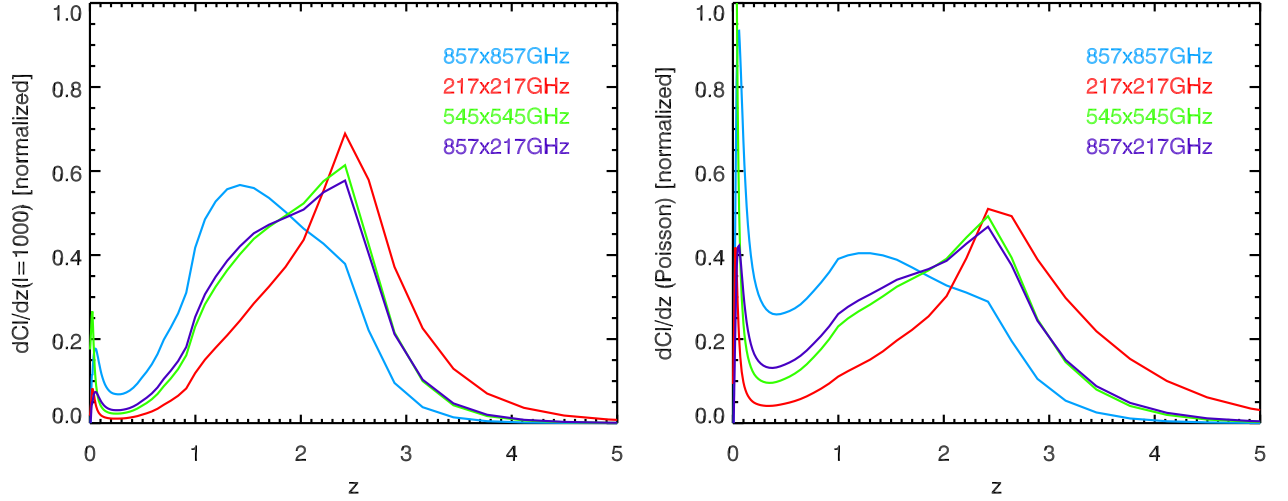


Fig. 12. Predicted redshift distribution of auto and cross power spectra at large ($\ell = 1000$, left) and small scale (Poisson level). We focus only on three frequencies: 857 GHz ($350\mu\text{m}$), 545 GHz ($550\mu\text{m}$), and 217 GHz ($1382\mu\text{m}$) to illustrate the difference between cross-spectrum between two distant wavelengths and the auto-spectrum at an intermediate wavelength.

Table 1. Predicted correlation of CIB anisotropies between bands at small scale (Poisson level, upper part) and large scale ($\ell=1000$, lower part).

Correlation between bands at small scales (Poisson)							
	3000 GHz	857 GHz	545 GHz	353 GHz	217 GHz	143 GHz	100 GHz
3000 GHz	1.000						
857 GHz	0.599	1.000					
545 GHz	0.407	0.916	1.000				
353 GHz	0.310	0.830	0.962	1.000			
217 GHz	0.277	0.785	0.920	0.968	1.000		
143 GHz	0.279	0.745	0.894	0.963	0.958	1.000	
100 GHz	0.333	0.743	0.881	0.940	0.921	0.988	1.000
Correlation between bands at large scale ($\ell=1000$)							
	3000 GHz	857 GHz	545 GHz	353 GHz	217 GHz	143 GHz	100 GHz
3000 GHz	1.000						
857 GHz	0.766	1.000					
545 GHz	0.636	0.971	1.000				
353 GHz	0.555	0.925	0.988	1.000			
217 GHz	0.529	0.902	0.975	0.997	1.000		
143 GHz	0.538	0.904	0.975	0.996	0.999	1.000	
100 GHz	0.575	0.919	0.981	0.996	0.997	0.999	1.000

higher redshift. At longer wavelengths, there is almost no evolution, because all the sources below $z \sim 7$ are seen in the Rayleigh-Jeans regime and the color is roughly the same at all redshifts. This trend is seen for both intensity and anisotropies, regardless of scale. There are, however, small differences between these three quantities. For instance, the redshift distribution of the Poisson level⁵ at $100\mu\text{m}$ is dominated by $z < 0.5$ sources, when a significant fraction of $\ell = 1000$ anisotropies is caused by galaxies at $z \sim 1$. This is due to the fact that the Poisson anisotropies are dominated by a small number of low- z bright galaxies just below the flux cut. Anisotropies at large scale are dominated by normal star-forming galaxies at $z \sim 1$ which dominate the background and the 2-halo term of anisotropies.

Finally, we checked that the redshift distributions predicted by our model agree with the lower limits derived by stacking of $24\mu\text{m}$ sources. We compare with the lower limits from Berta et al. (2011) at $100\mu\text{m}$, Jauzac et al. (2011) at $160\mu\text{m}$ and

B  thermin et al. (2012c) at $250\mu\text{m}$, $350\mu\text{m}$, and $500\mu\text{m}$, which well agree with our model. We also simulate with our model the selection corresponding to these various works and found a good overall agreement below $z \sim 2.5$. At larger redshift and for a $24\mu\text{m}$ selection, these predictions are underestimated. This is expected because our SED templates take only into account the dust emission, when $\lambda < 8\mu\text{m}$ rest-frame emission are significantly affected by stellar emissions. We thus underestimate the number of $24\mu\text{m}$ detections and consequently also their contribution to the CIB.

8.2. Redshift distribution of CIB cross-correlation between bands

Cross power spectra between bands provide complementary information to the auto-spectra. Fig. 12 shows the redshift distribution of a selection of cross and auto-spectra. At both large ($\ell = 1000$, left) and small scale (Poisson), the redshift distribution of the cross-spectra between two distant bands (e.g.

⁵ We used the same flux cuts as in Sect. 6

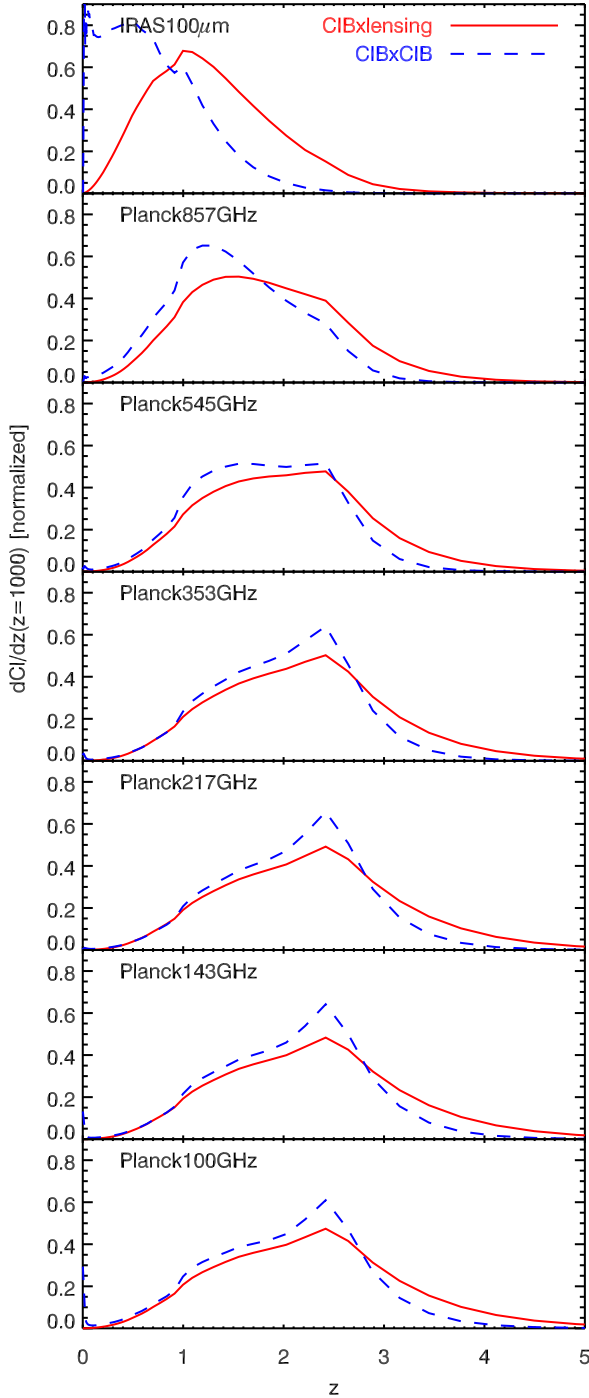


Fig. 13. Comparison between the predicted redshift distributions of CIBxLensing and CIBxLensing signal in various IRAS/Planck bands. *Red solid line:* Redshift distribution of the cross-correlation between CIB and CMB lensing at $\ell=1000$ in various bands. *Blue dashed line:* Redshift distribution of CIB auto-power-spectrum.

857 and 217 GHz here) is pretty close to the redshift distribution for an intermediate band (e.g. 545 GHz here), except for a difference of Poisson level at very low z caused by different flux cuts. Considering the quite fine spectral coverage of our data, we thus cannot claim that cross-spectra probe different redshift ranges.

In contrast, the correlation $(C_{\ell}^{yy'}/\sqrt{C_{\ell}^{yy} \times C_{\ell}^{y'y'}})$ between bands provides a useful test of the validity of the models (especially their SEDs and redshift distributions). This correlation varies with scale. We thus focused on Poisson level and $\ell = 1000$. The results are summarized in Table 1. The level of correlation is also important for cosmic microwave background (CMB) experiments to know whether or not the CIB at high frequency is a good proxy of the CIB emission at low frequency. For instance, the correlation between 857 GHz and 143 GHz is 0.904 at $\ell = 1000$, but only 0.75 for the Poisson level. This correlation is predicted to rise to 0.996 between 353 GHz and 143 GHz (0.963 for the Poisson level). According to our model, the CIB at 353 GHz thus provides a very good proxy for CIB in the CMB channels.

8.3. Redshift distribution of CIBxLensing signal

The cross-correlation between CIB and lensing provides supplementary information probing a slightly different redshift range. Fig. 13 shows a comparison between the predicted redshift distributions of the CIB auto-spectrum and the cross-spectrum between CIB and CMB lensing for various bands. While the redshift distribution of the auto-spectrum evolves strongly between 100 (3000 GHz) and 850 μm (353 GHz), this evolution is weaker for the cross-correlation with CMB lensing which mainly probes the $z = 1 - 2$ redshift range. CIBxLensing is thus a good probe of the mean SED of galaxies contributing to the CIB at this epoch. However, apart from 100 μm band, the redshift range probed by CIBxLensing is relatively similar to that of the CIB power spectrum, but it is an independent and more direct probe of the link between dark matter and star-forming objects, because the lensing of the CMB by the large scale structures is a very well known and modeled physical process.

9. Star formation and dark matter halos

In this section, we will discuss the prediction of our model in the context of our current understanding of galaxy formation. We use model C, as discussed in Sect. 7.

9.1. Evolution of infrared-light-to-mass ratio with redshift

The infrared-light-to-halo-mass ratio is a key ingredient of our CIB model. Fig. 14 shows this relation for various hypotheses. We consider two different definitions of the infrared luminosity inside the halos: the infrared luminosity of a central galaxy lying exactly at the core of the main-sequence (top panels) and the mean infrared luminosity of central galaxies (lower panels) hosted by halos of a given mass. This second quantity takes into account the fact that a fraction of galaxies are passive, while the first quantity takes into account only the star-forming galaxies. We also use both the instantaneous halo mass (left panels) and the halo mass at $z=0$. The conversion between instantaneous halo mass and halo mass at $z=0$ is performed assuming an accretion following the fits of Fakhouri & Ma (2010) to their own

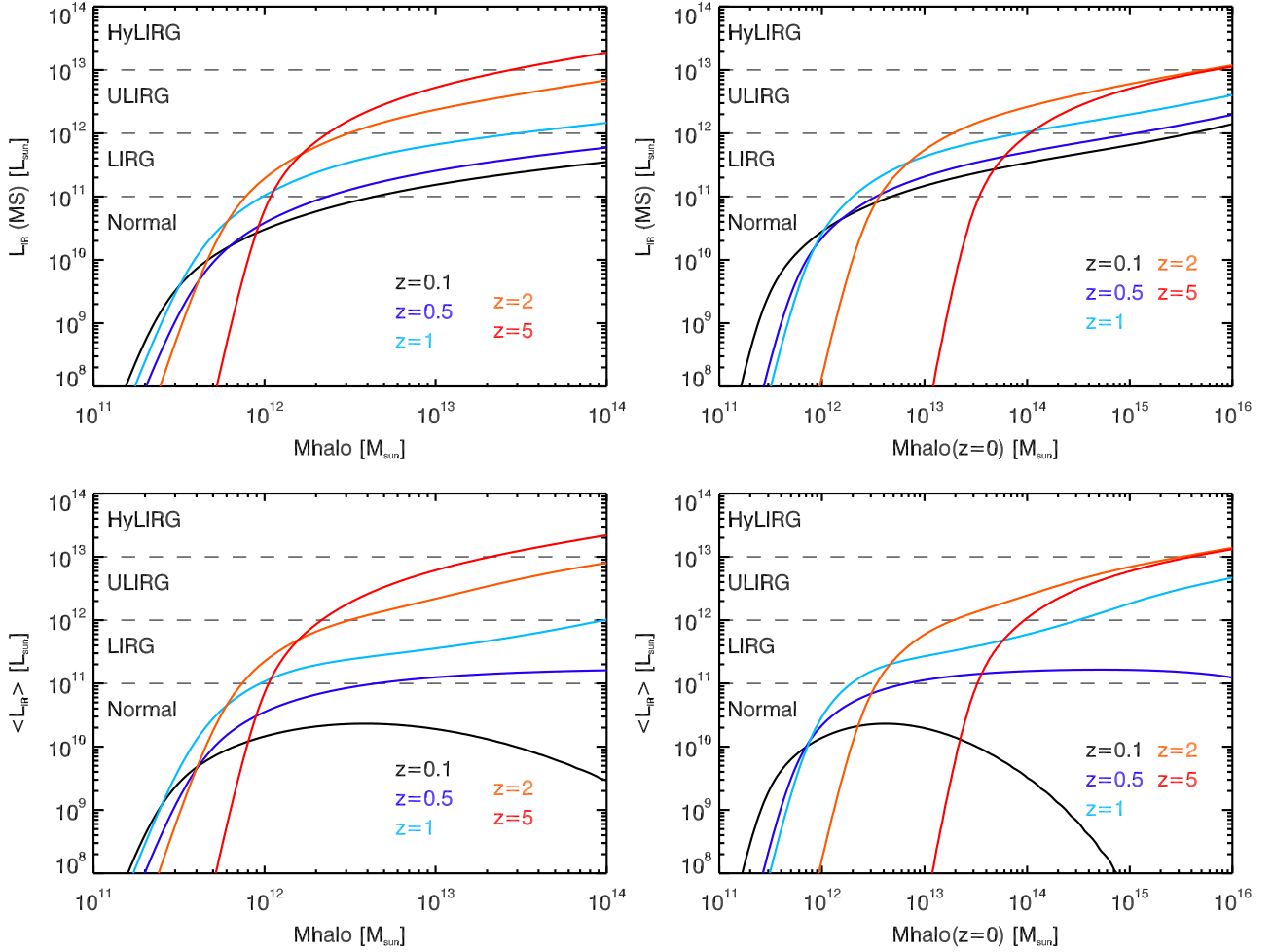


Fig. 14. Relation between infrared luminosity of galaxies and their halo mass. The *top* panels correspond to the infrared luminosity for a central galaxy exactly on the main-sequence. The *bottom* panels shows the mean infrared luminosity of the central galaxies. The *left* panels shows results as the instantaneous halo mass and *right panel* as a function of halo mass at $z=0$. The dashed lines correspond to the limit between normal galaxies (i.e. $< 10^{11} L_{\odot}$), LIRGs ($10^{11} < L_{\text{IR}} < 10^{12} L_{\odot}$), ULIRGs ($10^{12} < L_{\text{IR}} < 10^{13} L_{\odot}$) and HyLIRGs ($> 10^{13} L_{\odot}$).

numerical simulations of dark matter:

$$\langle \dot{M}_h \rangle = 46.1 \times M_{\odot} / \text{yr}^{-1} \left(\frac{M_h}{10^{12} M_{\odot}} \right)^{1.1} \times (1 + 1.11z) \times \sqrt{\Omega_m(1+z)^3 + \Omega_{\Lambda}}. \quad (34)$$

The mass at $z=0$ ($M_h(z) + \int_{t(z'=z)}^{t(z'=0)} \langle \dot{M}_h \rangle dt$) is a convenient quantity to use when discussing the evolution of structures with time.

The shape of the infrared luminosity as a function of instantaneous halo mass evolves little with redshift. However, its normalization varies strongly. For the same halo mass, infrared luminosity is much more intense at high redshift. This results will be interpreted further in Sect. 9.3. At low mass, the infrared luminosity decreases quickly for several reasons. The main cause is the low star formation efficiency in low-mass halos (e.g. Behroozi et al. 2012a; Leauthaud et al. 2012). In addition, low-mass galaxies are less attenuated than massive ones, such that only a small fraction of the UV photons emitted by young star is reprocessed into infrared light (e.g. Pannella et al. 2009; Sobral et al. 2013). At high mass, we found a sub-linear relation, even if we consider only objects on

the main-sequence. This implies that mechanisms of feedback are pretty efficient in massive halos. This trend is stronger if we consider the mean infrared luminosity taking into account the quenched galaxies. At $z < 1$, the infrared luminosity decreases when halo mass becomes larger than $10^{13} M_{\odot}$, and our model thus predicts a very weak star-formation in dense environment at low redshift in agreement with e.g. Feruglio et al. (2010). The contribution of satellites is small except in massive halos ($> 10^{13} M_{\odot}$), where the central is inefficient in forming stars.

The infrared luminosity as a function of halo mass at $z=0$ exhibits a strong downsizing. The progenitors of $10^{14} M_{\odot}$ initially host a very intense star formation rate (ULIRG regime, $10^{12} < L_{\text{IR}} < 10^{13} L_{\odot}$) at high redshift ($z=5$) which continues to grow up to $z \sim 2$. Then, the infrared luminosity decreases because star formation is less efficient in massive halos (see Sect. 9.3). The less massive halos need more time to ignite intense star formation. Dark matter halos similar to that of MilkyWay ($\sim 10^{12} M_{\odot}$ at $z=0$) host significant infrared emission only below $z=1$.

We can compare the predictions of our model with estimates based on clustering of various samples of galaxies. Sub-millimeter galaxies (defined here to have $S_{850} > 3 \text{ mJy}$)

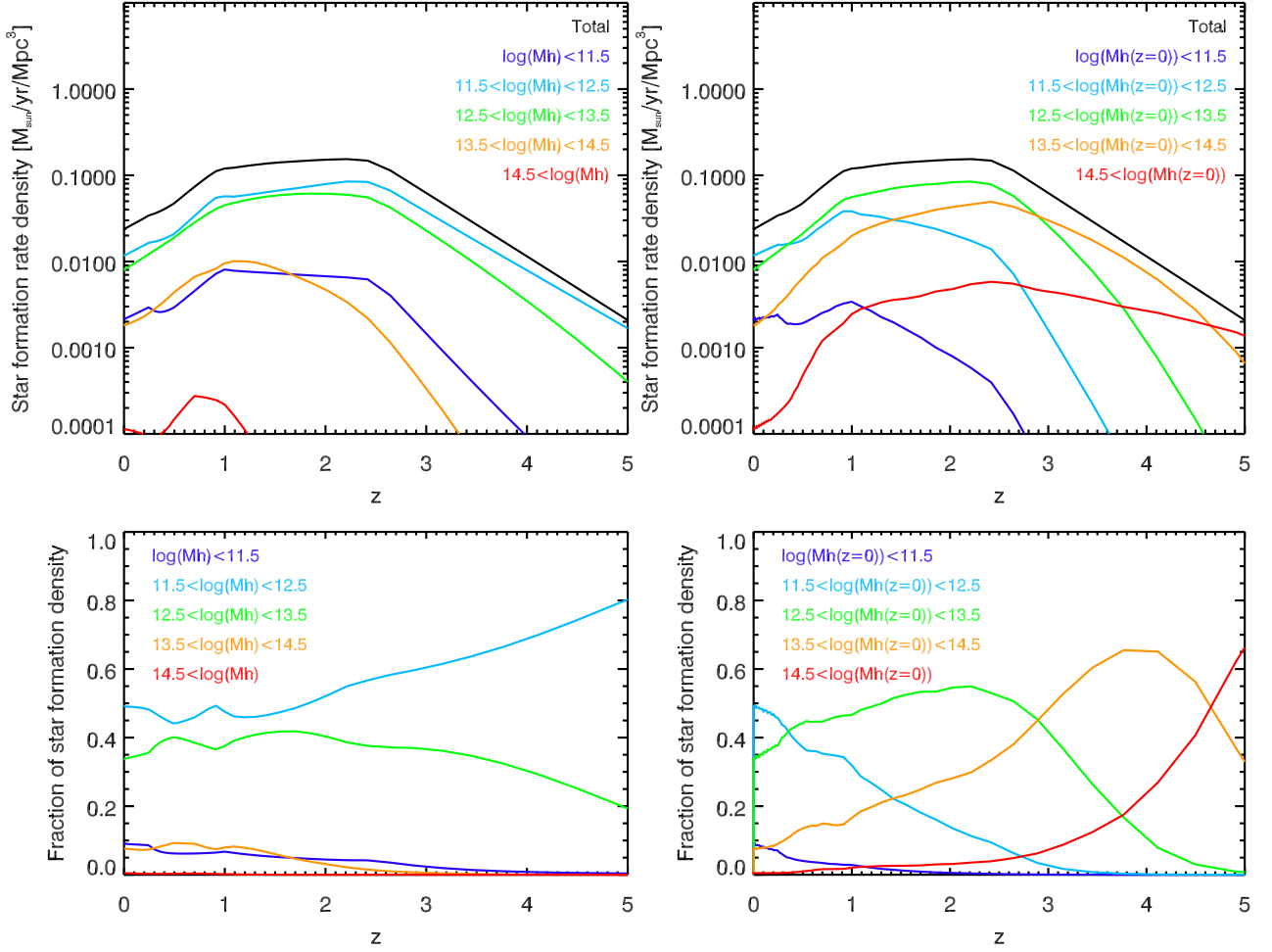


Fig. 15. Contribution of various halo mass to the star formation history. *Upper panels* shows the contribution of each slice to star formation density and *lower panels* their fractional contribution. We use slice of instantaneous halo mass in the *left panels* and mass at $z=0$ in the *right panels*.

are essentially ULIRGs at $z \sim 2.4$ (e.g. Chapman et al. 2003) and the B12 model predicts that these objects generally lie on the main-sequence. Blain et al. (2004) showed that the correlation length of SMGs is compatible with typical host halos of $10^{13} M_{\odot}$, which is consistent with our model prediction of an infrared luminosity of $4 \times 10^{12} L_{\odot}$ for a main-sequence galaxy in a $10^{13} M_{\odot}$ halo at $z=2.4$ (see Fig. 14). We can also check the consistency of our results with measurements based on *Spitzer* $24 \mu\text{m}$ observations. Magliocchetti et al. (2008) measured the clustering of two samples of sources with $S_{24} > 400 \mu\text{Jy}$ with a mean redshift of 0.79 and 2.02, respectively. This flux selection corresponds, at the mean redshift of each sample, to an infrared luminosity of $2.6 \times 10^{11} L_{\odot}$ and $2.6 \times 10^{12} L_{\odot}$, respectively for a main-sequence SED. For an object exactly on the main sequence, this corresponds to an instantaneous halo mass of $2.7 \times 10^{12} M_{\odot}$ and $1.2 \times 10^{13} M_{\odot}$, in agreement with the minimal mass found by Magliocchetti et al. (2008) of $0.8^{+2.3}_{-0.7} \times 10^{12} M_{\odot}$ and $0.6^{+0.6}_{-0.3} \times 10^{13} M_{\odot}$, respectively. Farrah et al. (2006) measured the halo mass of $5.8 \mu\text{m}$ IRAC peakers with $24 \mu\text{m}$ detections and found a 1σ range for $\log(M_h)$ of 13.7–14.1. This population of massive star-forming galaxies has a mean redshift of 2.017 and a mean infrared luminosity of $8.9 \pm 0.6 L_{\odot}$ (Fiolet et al. 2010), which is associated in our model to $\log(M_h)=14.1$.

9.2. Contribution of various halo masses to star formation history

The total star-formation rate of both central and satellite galaxies hosted by a given halo can be derived from our model. In combination with the halo mass function, we can then compute the contribution of each halo mass to the star formation rate. The results of this analysis are presented Fig. 15. If we consider instantaneous halo mass (left panels), the bulk of the star formation is hosted by halos between $10^{11.5} M_{\odot}$ and $10^{13.5} M_{\odot}$ regardless the redshift, suggesting the existence of a characteristic mass which favors star-formation. The fractional contribution of each mass slice is inferred to have evolved slowly with redshift, except at $z > 3$. However, there are significant uncertainties in the behavior of the galaxies at high redshift and these results should be taken with caution.

Because of the growth of dark matter halos, the same halo mass at various redshifts corresponds to progenitors of different type of halos. In order to take this into account, we also considered slices of $z=0$ halo mass (right panels). The star formation rate density is predicted to have been successively dominated by progenitors of massive clusters ($M_h > 10^{14.5} M_{\odot}$) at $z > 4.7$, small clusters and large group ($10^{13.5} < M_h < 10^{14.5} M_{\odot}$) at $2.8 < z < 4.7$, small groups

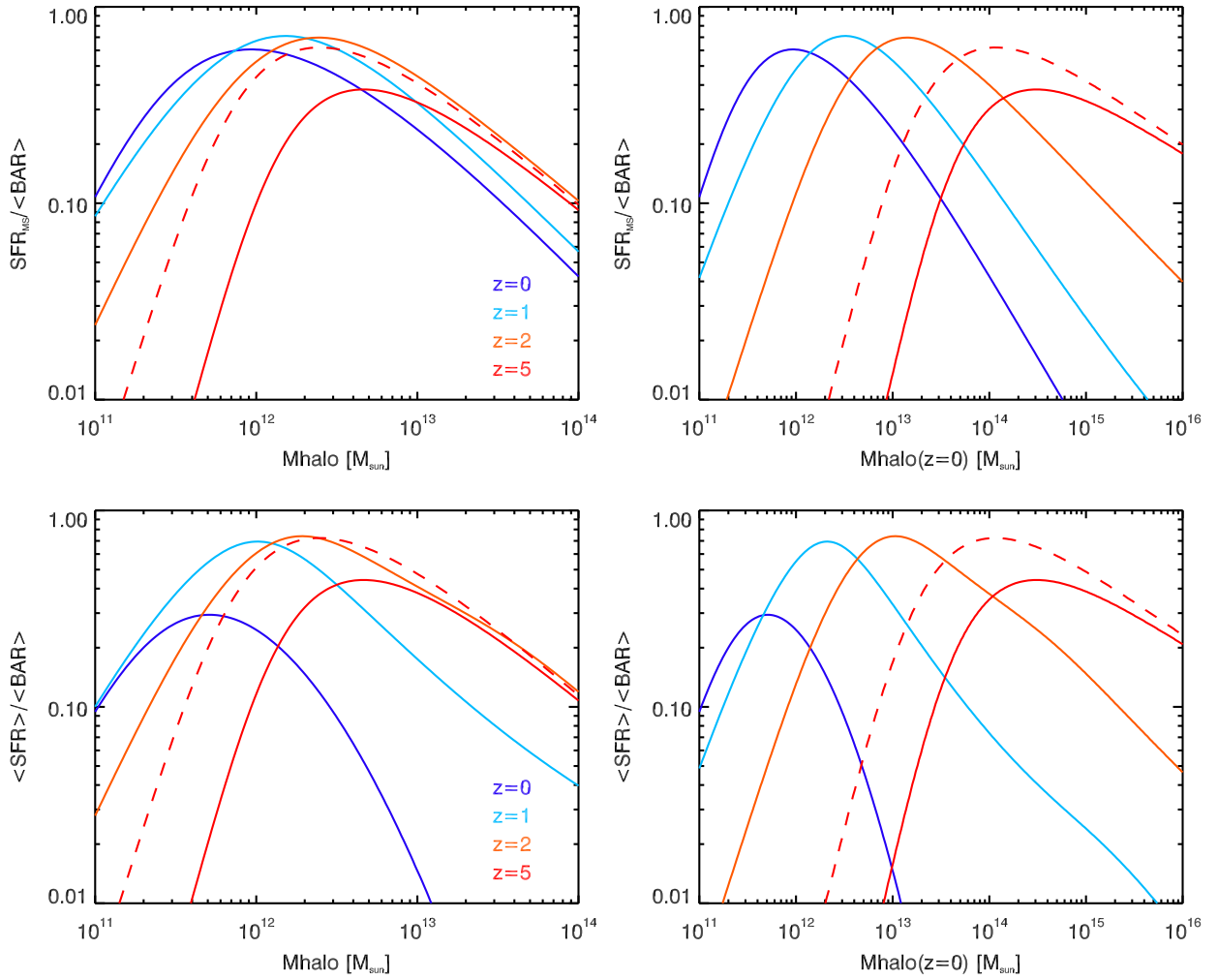


Fig. 16. Instantaneous star formation efficiency (defined here as SFR/BAR , where BAR is the baryonic accretion rate) as a function of halo mass at various redshift predicted by our model. The predictions from model C are plotted with a solid line. At $z = 5$ model A predicts a different efficiency distribution and is represented by a dashed line. *Upper panels* shows this efficiency only for main-sequence galaxies and *lower panels* for mean efficiency. We use slice of instantaneous halo mass in the *left panels* and mass at $z=0$ in the *right panels*.

($10^{12.5} < M_h < 10^{13.5} M_\odot$) at $0.5 < z < 2.8$, and Milky Way-like halos ($10^{11.5} < M_h < 10^{12.5} M_\odot$) at $z < 0.5$. Star-formation thus initially occurs in the progenitor of the most massive halos before becoming less efficient, and then propagating to less massive halos. This strong downsizing explains why the star formation rate densities at redshift 1 and 2 are similar. $z > 2$ infrared luminosity density is dominated by a small density ($\sim 3 \times 10^{-3} \text{ Mpc}^{-4}$) of ULIRGs and $z \sim 1$ is dominated by a larger density ($\sim 3 \times 10^{-3} \text{ Mpc}^{-3}$) of LIRGs (e.g. Béthermin et al. 2011).

9.3. Efficiency of star formation as a function of halo mass and redshift

To conclude, we derive an estimate of the instantaneous star formation efficiency (ISFE) in different halos by computing the ratio between SFR and baryonic accretion rate (BAR). Here, we assume the BAR to be the total matter accretion as given by Fakhouri & Ma (2010) multiplied by the universal baryonic fraction ($\text{BAR} = \langle \dot{M}_h \rangle \times \Omega_b / \Omega_m$ with $\langle \dot{M}_h \rangle$ defined in Eq. 34). This simplified definition neglects the fact that the gas is not

transformed instantaneously into stars and large gas reservoirs are present in (e.g. Daddi et al. 2010; Tacconi et al. 2012) and around (Cantalupo et al. 2012) high- z galaxies. Fig. 16 shows predictions for the variation of this efficiency as a function of halo mass at various redshift. Star-formation efficiency in main-sequence galaxies as a function of instantaneous halo mass (upper left panel) slowly evolves between $z=0$ and $z=2$ with a slight increase of the mass of maximum efficiency with redshift (from $8 \times 10^{11} M_\odot$ at $z=0$ to $3 \times 10^{12} M_\odot$ at $z=2$). At $z=5$, this maximal efficiency is smaller and the halo mass where it occurs is higher. The increase of the mass of maximum efficiency could be due to a delay in the ignition of star-formation activity, because the BAR in $\sim 10^{12} M_\odot$ halos is higher at high redshift. However, large uncertainties exist at high redshift where we have few constraints on star-forming galaxies. For instance, if we use model A (flat sSFR at $z > 2.5$) instead of model C (rising sSFR) to perform our calculations this effect is much smaller (dashed line in Fig. 16). Below the mass-scale at which peak efficiency is reached, the gravitational potential of the halo is lower and supernova feedback is probably sufficiently strong to remove gas from the galaxy (e.g. Silk 2003; Bertone et al. 2005). At higher masses, the slow decrease of the star formation

efficiency could be caused by the transition from cold streams below $M_h \sim 10^{12} M_\odot$ to isotropic cooling above this mass (e.g. Dekel & Birnboim 2006; Faucher-Gigu  re et al. 2011). At high mass, the cooling time of gas becomes much longer than the free fall time because of the hot atmosphere in the massive halos (e.g. Kere  s et al. 2005; Birnboim et al. 2007). Contrary to the ISFE in main sequence galaxies, the mean ISFE (lower left panel), that takes into account the fact that a fraction of galaxies are quenched, exhibits a strong break at $M_h > 10^{12} M_\odot$ at $z = 0$ and a moderate break at the same mass at $z = 1$. This break could be caused by a suppression of isotropic gas cooling by energy injection in the halo atmosphere by active galactic nuclei (AGN) activity (e.g. Cattaneo et al. 2006; Somerville et al. 2008; Ostriker et al. 2010).

Regardless of the redshift and halo mass, the SFR in main-sequence galaxies is always lower than the BAR onto the dark matter halos (see Fig. 16). For a Chabrier (2003) IMF, the maximal efficiency is ~ 0.7 . Appendix C discusses the case of a Salpeter (1955) IMF. This is consistent with the standard assumption that main-sequence galaxies host secular star-formation. This is not the case for episodic starbursts, which on average forms 4 times more stars for the same halo mass than main-sequence galaxies and thus transform much more gas into stars than they receive from cosmic accretion. They thus tend to exhaust their gas reservoir rapidly. The fact that main-sequence galaxies do not need to store gas to fuel their star-formation could seem in contradiction with the fact that the specific halo growth rate (sHGR) is larger by a factor of two than the sSFR around $z = 2$, as pointed out by Weinmann et al. (2011). However, the ratio between sSFR and sHGR is:

$$\frac{\text{SFR}/M_\star}{\dot{M}_h/M_h} = \frac{\eta \dot{M}_b/\dot{M}_h}{M_\star/M_h} = \eta \frac{M_b}{M_\star}, \quad (35)$$

where η is the instantaneous star formation efficiency (SFR/\dot{M}_b), M_b the baryonic accretion into the halo. The ratio between sSFR and sHGR can thus be much higher than unity in halos of $\sim 10^{12} M_\odot$, because, even if η is lower than 1, the ratio between baryonic mass and stellar mass is ~ 4 (e.g. Leauthaud et al. 2012), because of the low efficiency of conversion of baryons into stars in the past (when the halos had a lower mass and thus a lower ISFE).

We can also discuss how the efficiency varies as a function of $z=0$ halo mass (right panels). We predict a strong evolution of the typical halos where the ISFE is maximal. The progenitors of massive halos form stars very efficiently at high redshift, while Milky-Way-like halos are very inefficient. The opposite trend is expected at low redshift. This picture is consistent with the strong downsizing of the star-forming galaxy population discussed in the previous sections, but also with the work Behroozi et al. (2012b). Their analysis was based only on the evolution of the SMF and SFR were derived assuming a single galaxy population. Our approach is based on the infrared observations which directly probe the SFR in galaxies and which take into account the diversity of galaxies using three distinct populations: secularly star-forming galaxies on the main-sequence, episodic, merger-driven starbursts and passive elliptical galaxies. Compared to Behroozi et al. (2012a), our mean ISFE is much lower in local massive halos, which almost exclusively host quenched galaxies, but we agree with their estimate if we take only a main-sequence population (more consistent with their single galaxy population).

Normal spiral galaxies at $z = 0$, LIRGs at $z = 1$, and ULIRGs at $z = 2$ dominate the star-formation density at these redshift and are essentially main sequence galaxies (Sargent et al. 2012). All of these are hosted by halos of similar mass associated, which are characterized by a very efficient conversion of accreted baryons into stars. The huge difference between their star formation rate can thus be explained by the accretion, which is stronger at high redshift. These objects can thus be viewed as different facets of the same universal process of secular star formation.

10. Conclusion

We have studied the connection between star formation and dark matter halos focusing on infrared observations. We developed a new modeling approach based on the 2SFM framework, which was already able to reproduce successfully the infrared luminosity function and number counts (Sargent et al. 2012, B12). This framework links stellar mass with star formation and infrared properties, assuming two different modes of star formation in secularly star-forming galaxies and episodic starbursts. We extended this formalism to the connection between stellar mass and halo mass using the technique of abundance matching. Our formalism account for the fact that a significant fraction of massive galaxies are passive and do not form stars (especially at low redshift).

- We developed a method to compute the CIB anisotropies (including power-spectra between different frequencies), the cross-correlation between CIB and CMB lensing, and auto-correlation functions of bright resolved galaxies using the prescription of the 2SFM formalism. To perform this computation, we produced effective SEDs of all galaxies at a given redshift which are available online⁶.
- We find that a slowly rising sSFR at $z > 2.5$ and a quenching of satellite of massive passive galaxies at low redshift (our model C), matches reasonably well the infrared data suggesting that this model is a valid description of the link between infrared galaxies and dark matter halos. The other versions of the model with flat sSFR and no quenching of satellites show some little discrepancies with the power-spectra, but cannot be conclusively ruled out.
- Our model is able to predict the redshift distribution of CIB anisotropies. We found that the mean redshift where the CIB is emitted varies strongly between $100 \mu\text{m}$ and $850 \mu\text{m}$ but only little at longer wavelengths. Consequently, the CIB anisotropies in the various bands above $850 \mu\text{m}$ are strongly correlated (> 0.9).
- We found a quick rise of the far-infrared-light-to-mass ratio with redshift in $M_h > 10^{12} M_\odot$ halos and a strong break at lower mass at all redshifts. We found that more than 90% of the star formation is hosted by halos with masses between $10^{11.5}$ and $10^{13.5} M_\odot$ at all redshifts. The progenitors of clusters ($M_h(z = 0) > 10^{13.5} M_\odot$) host the bulk of the star-formation at $z > 3$. Star formation activity then propagates to groups ($10^{12.5} < M_h(z = 0) < 10^{13.5} M_\odot$) at $0.5 < z < 3$ and Milky Way-like halos ($10^{11.5} < M_h(z = 0) < 10^{12.5} M_\odot$) at $z < 0.5$. We also found that there is a characteristic halo mass ($\sim 10^{12} M_\odot$) where the star formation efficiency is maximal ($\sim 70\%$ at all redshift). The large difference of SFR in galaxies dominating the background at low and high redshift would thus be driven by a difference of accretion rate in the halos close to this mass.

⁶ <http://irfu.cea.fr/Sap/Phoceia/Page/index.php?id=537>

Our simple modeling framework is very efficient in explaining the current observations of the infrared Universe. However, future large sub-millimeter surveys (e.g. NIKA, CCAT) will resolve the bulk of the CIB into individual sources and will probably improve measurements of the clustering properties of infrared galaxies. We expect that deviation from our model will appear at small scales, where environmental effects could have a strong impact, thereby revealing a more complex and varied infrared Universe.

Acknowledgements. We thank Steve Maddox for providing data and discussion about clustering measurements, Marco Viero and Amir Hajian for providing data, and Paolo Serra for useful discussion. MB, ED, and MS acknowledge for the support provided by the grants ERC-StG UPGAL 240039 and ANR-08-JCJC-0008. LW acknowledges support from an ERC StG grant (DEGAS-259586). This research was carried out in part at the Jet Propulsion Laboratory, run by the California Institute of Technology under a contract from NASA.

References

Addison, G. E., Dunkley, J., & Bond, J. R. 2012, ArXiv e-prints
Amblard, A. & Cooray, A. 2007, ApJ, 670, 903
Amblard, A., Cooray, A., Serra, P., et al. 2011, Nature, 470, 510
Behroozi, P. S., Conroy, C., & Wechsler, R. H. 2010, ApJ, 717, 379
Behroozi, P. S., Wechsler, R. H., & Conroy, C. 2012a, ArXiv e-prints
Behroozi, P. S., Wechsler, R. H., & Conroy, C. 2012b, ArXiv e-prints
Berta, S., Magnelli, B., Nordon, R., et al. 2011, A&A, 532, A49
Bertone, S., Stoehr, F., & White, S. D. M. 2005, MNRAS, 359, 1201
Béthermin, M., Daddi, E., Magdis, G., et al. 2012a, ApJ, 757, L23
Béthermin, M., Dole, H., Beelen, A., & Aussel, H. 2010a, A&A, 512, A78+
Béthermin, M., Dole, H., Cousin, M., & Bavouzet, N. 2010b, A&A, 516, A43+
Béthermin, M., Dole, H., Lagache, G., Le Borgne, D., & Penin, A. 2011, A&A, 529, A4+
Béthermin, M., Doré, O., & Lagache, G. 2012b, A&A, 537, L5
Béthermin, M., Le Floch, E., Ilbert, O., et al. 2012c, A&A, 542, A58
Birnbom, Y., Dekel, A., & Neistein, E. 2007, MNRAS, 380, 339
Blain, A. W., Chapman, S. C., Smail, I., & Ivison, R. 2004, ApJ, 611, 725
Cantalupo, S., Lilly, S. J., & Haehnelt, M. G. 2012, MNRAS, 425, 1992
Cattaneo, A., Dekel, A., Devriendt, J., Guiderdoni, B., & Blaizot, J. 2006, MNRAS, 370, 1651
Chabrier, G. 2003, PASP, 115, 763
Challinor, A. & Lewis, A. 2005, Phys. Rev. D, 71, 103010
Chapman, S. C., Blain, A. W., Ivison, R. J., & Smail, I. R. 2003, Nature, 422, 695
Condon, J. J. 1974, ApJ, 188, 279
Conroy, C. & Wechsler, R. H. 2009, ApJ, 696, 620
Cooray, A., Amblard, A., Wang, L., et al. 2010, A&A, 518, L22+
Cooray, A. & Sheth, R. 2002, Phys. Rep., 372, 1
Daddi, E., Bournaud, F., Walter, F., et al. 2010, ApJ, 713, 686
Daddi, E., Dickinson, M., Morrison, G., et al. 2007, ApJ, 670, 156
de Barros, S., Schaerer, D., & Stark, D. P. 2012, ArXiv e-prints
De Bernardis, F. & Cooray, A. 2012, ArXiv e-prints
Dekel, A. & Birnbom, Y. 2006, MNRAS, 368, 2
Dole, H., Lagache, G., Puget, J., et al. 2006, A&A, 451, 417
Dole, H., Le Floch, E., Pérez-González, P. G., et al. 2004, ApJS, 154, 87
Elbaz, D., Daddi, E., Le Borgne, D., et al. 2007, A&A, 468, 33
Fakhouri, O. & Ma, C.-P. 2010, MNRAS, 401, 2245
Farrah, D., Lonsdale, C. J., Borys, C., et al. 2006, ApJ, 643, L139
Faucher-Giguère, C.-A., Kereš, D., & Ma, C.-P. 2011, MNRAS, 417, 2982
Feruglio, C., Aussel, H., Le Floch, E., et al. 2010, ApJ, 721, 607
Fiolet, N., Omont, A., Lagache, G., et al. 2010, A&A, 524, A33
Fixsen, D. J., Dwek, E., Mather, J. C., Bennett, C. L., & Shafer, R. A. 1998, ApJ, 508, 123
Franceschini, A., Rodighiero, G., Vaccari, M., et al. 2010, A&A, 517, A74+
Glenn, J., Conley, A., Béthermin, M., et al. 2010, MNRAS, 409, 109
Gonzalez, V., Bouwens, R., Ilingworth, G., et al. 2012, ArXiv e-prints
Grossan, B. & Smoot, G. F. 2007, A&A, 474, 731
Grupponi, C., Pozzi, F., Zamorani, G., & Vignali, C. 2011, MNRAS, 416, 70
Hajian, A., Viero, M. P., Addison, G., et al. 2011, ArXiv e-prints
Hall, N. R., Keisler, R., Knox, L., et al. 2010, ApJ, 718, 632
Hanson, D., Rocha, G., & Górski, K. 2009, MNRAS, 400, 2169
Hauser, M. G., Arendt, R. G., Kelsall, T., et al. 1998, ApJ, 508, 25
Hauser, M. G. & Dwek, E. 2001, ARA&A, 39, 249
Ilbert, O., McCracken, H. J., Le Fevre, O., et al. 2013, ArXiv e-prints
Ilbert, O., Salvato, M., Le Floch, E., et al. 2010, ApJ, 709, 644

Jauzac, M., Dole, H., Le Floch, E., et al. 2011, A&A, 525, A52+
Kennicutt, Jr., R. C. 1998, ApJ, 498, 541
Kereš, D., Katz, N., Weinberg, D. H., & Davé, R. 2005, MNRAS, 363, 2
Kim, H.-S., Lacey, C. G., Cole, S., et al. 2012, MNRAS, 425, 2674
Knox, L., Cooray, A., Eisenstein, D., & Haiman, Z. 2001, ApJ, 550, 7
Lagache, G., Bavouzet, N., Fernandez-Conde, N., et al. 2007, ApJ, 665, L89
Lagache, G., Dole, H., & Puget, J.-L. 2003, MNRAS, 338, 555
Lagache, G., Haffner, L. M., Reynolds, R. J., & Tufte, S. L. 2000, A&A, 354, 247
Lagache, G., Puget, J., & Dole, H. 2005, ARA&A, 43, 727
Lapi, A., González-Nuevo, J., Fan, L., et al. 2011, ApJ, 742, 24
Larson, D., Dunkley, J., Hinshaw, G., et al. 2010, ArXiv e-prints
Le Borgne, D., Elbaz, D., Ocvirk, P., & Pichon, C. 2009, A&A, 504, 727
Leauthaud, A., George, M. R., Behroozi, P. S., et al. 2012, ApJ, 746, 95
Maddox, S. J., Dunne, L., Rigby, E., et al. 2010, A&A, 518, L11
Magdis, G. E., Daddi, E., Béthermin, M., et al. 2012, ApJ, 760, 6
Magliocchetti, M., Cirasuolo, M., McLure, R. J., et al. 2008, MNRAS, 383, 1131
Magliocchetti, M., Santini, P., Rodighiero, G., et al. 2011, MNRAS, 416, 1105
Marsden, G., Ade, P. A. R., Bock, J. J., et al. 2009, ApJ, 707, 1729
Marsden, G., Chapin, E. L., Halpern, M., et al. 2011, MNRAS, 417, 1192
Mazin, D. & Raue, M. 2007, A&A, 471, 439
More, S., van den Bosch, F. C., Cacciato, M., et al. 2009, MNRAS, 392, 801
Moster, B. P., Somerville, R. S., Maubetsch, C., et al. 2010, ApJ, 710, 903
Navarro, J. F., Frenk, C. S., & White, S. D. M. 1997, ApJ, 490, 493
Nguyen, H. T., Schulz, B., Levenson, L., et al. 2010, A&A, 518, L5
Noeske, K. G., Weiner, B. J., Faber, S. M., et al. 2007, ApJ, 660, L43
Oliver, S. J., Wang, L., Smith, A. J., et al. 2010, A&A, 518, L21+
Ostriker, J. P., Choi, E., Ciotti, L., Novak, G. S., & Proga, D. 2010, ApJ, 722, 642
Pannella, M., Carilli, C. L., Daddi, E., et al. 2009, ApJ, 698, L116
Papovich, C., Dole, H., Egami, E., et al. 2004, ApJS, 154, 70
Park, C., Choi, Y.-Y., Vogeley, M. S., et al. 2007, ApJ, 658, 898
Patanchon, G., Ade, P. A. R., Bock, J. J., et al. 2009, ApJ, 707, 1750
Pénin, A., Doré, O., Lagache, G., & Béthermin, M. 2012a, A&A, 537, A137
Pénin, A., Lagache, G., Noriega-Crespo, A., et al. 2012b, A&A, 543, A123
Planck Collaboration, Ade, P. A. R., Aghanim, N., et al. 2013, ArXiv e-prints
Planck Collaboration, Ade, P. A. R., Aghanim, N., et al. 2011, ArXiv e-prints
Puget, J., Abergel, A., Bernard, J., et al. 1996, A&A, 308, L5+
Rahmati, A. & van der Werf, P. P. 2011, MNRAS, 418, 176
Rodighiero, G., Daddi, E., Baronchelli, I., et al. 2011, ApJ, 739, L40
Salpeter, E. E. 1955, ApJ, 121, 161
Sargent, M. T., Béthermin, M., Daddi, E., & Elbaz, D. 2012, ApJ, 747, L31
Sargent, M. T., Daddi, E., Béthermin, M., et al. 2013, ArXiv e-prints
Schechter, P. 1976, ApJ, 203, 297
Shang, C., Haiman, Z., Knox, L., & Oh, S. P. 2012, MNRAS, 421, 2832
Silk, J. 2003, MNRAS, 343, 249
Sobral, D., Smail, I., Best, P. N., et al. 2013, MNRAS, 428, 1128
Somerville, R. S., Hopkins, P. F., Cox, T. J., Robertson, B. E., & Hernquist, L. 2008, MNRAS, 391, 481
Stark, D. P., Schenker, M. A., Ellis, R. S., et al. 2012, ArXiv e-prints
Tacconi, L. J., Neri, R., Genzel, R., et al. 2012, ArXiv e-prints
Teplitz, H. I., Chary, R., Elbaz, D., et al. 2011, AJ, 141, 1
Tinker, J., Kravtsov, A. V., Klypin, A., et al. 2008, ApJ, 688, 709
Tinker, J. L. & Wetzel, A. R. 2010, ApJ, 719, 88
Vale, A. & Ostriker, J. P. 2004, MNRAS, 353, 189
Valiante, E., Lutz, D., Sturm, E., Genzel, R., & Chapin, E. L. 2009, ApJ, 701, 1814
Viero, M. P., Ade, P. A. R., Bock, J. J., et al. 2009, ApJ, 707, 1766
Viero, M. P., Wang, L., Zemcov, M., et al. 2012, ArXiv e-prints
Wang, L., Farrah, D., Oliver, S. J., et al. 2012, ArXiv e-prints
Watson, D. F. & Conroy, C. 2013, ArXiv e-prints
Weinmann, S. M., Neistein, E., & Dekel, A. 2011, MNRAS, 417, 2737
Xia, J.-Q., Negrello, M., Lapi, A., et al. 2012, MNRAS, 422, 1324
Zemcov, M., Blain, A., Halpern, M., & Levenson, L. 2010, ApJ, 721, 424

Appendix A: Conversions tables

Appendix A.1: Wavenumber, multipole, and angle

On small scales (*Spitzer*, *Herschel*), where curvature of the sky is negligible, people uses in general wavenumber (k) in their measurements of CIB power-spectrum. This is not the case for large-scale measurements (SPT, ACT, *Planck*) for which people used mutlitpole (ℓ). The conversion between the two is just $\ell = 2\pi k$. This also corresponds to a characteristic angular scale $\theta = \pi/\ell$. Table A.1 provides conversion for the range of values used in this paper.

Table A.1. Conversion between wavenumber, multipole, and angle

Multipole ℓ	Wavenumber k	Angle θ
	arcmin ⁻¹	degree
1	0.00005	180.00000
2	0.00009	90.00000
5	0.00023	36.00000
10	0.00046	18.00000
20	0.00093	9.00000
50	0.00231	3.60000
100	0.00463	1.80000
200	0.00926	0.90000
500	0.02315	0.36000
1000	0.04630	0.18000
2000	0.09259	0.09000
5000	0.23148	0.03600
10000	0.46296	0.01800
20000	0.92593	0.00900
50000	2.31481	0.00360
100000	4.62963	0.00180

Table A.2. Conversion between wavelength and frequency for various passbands used in this paper

Wavelength μm	Frequency GHz
24	12500
100	3000
160	1875
250	1200
350	857
500	600
550	545
850	353
1100	272
1382	217
2097	143
3000	100

Appendix A.2: From wavelengths to frequencies

Infrared astronomers use wavelengths in μm , the CMB community frequencies in GHz. For quick reference, we here provide in Table A.2 the conversion between these two conventions for the passbands discussed in this paper.

Appendix B: Computation of the cross-Poisson term

The number of sources per steradian n_{ij} with an infrared luminosity in the interval $[L_{\text{IR},i}, L_{\text{IR},i} + \Delta L_{\text{IR},i}]$ and a redshift in $[z_j, z_j + \Delta z_j]$ is:

$$n_{ij} = \frac{dV}{dz} \times \frac{d^2N}{dL_{\text{IR}}dV} \times \Delta L_{\text{IR},i} \Delta z_j. \quad (\text{B.1})$$

We also need to separate the galaxies by mode of star formation (main-sequence or starburst) and $\langle U \rangle$ parameter. The number of main-sequence or starburst galaxies $n_{ijk}^{\text{MS or SB}}$ in the same L_{IR} and z bins and with $\langle U \rangle$ in $[\langle U \rangle_k, \langle U \rangle_k + \Delta \langle U \rangle_k]$ is:

$$n_{ijk}^{\text{MS or SB}} = \frac{dV}{dz} \times \frac{d^2N}{dL_{\text{IR}}dV} \times \Delta L_{\text{IR},i} \Delta z_j \times p_{\text{MS or SB}}(\langle U \rangle) \times \Delta \langle U \rangle_k.$$

Since we assume Poisson statistics, the variance on the number of galaxies in this bin equals $n_{ijk}^{\text{MS or SB}}$. For the co-variance between the fluxes at the two frequencies caused by this sub-population we have:

$$\sigma_{S_\nu S_{\nu'}, ijk}^{\text{MS or SB}} = S_\nu \times S_{\nu'} \times n_{ijk} = L_{\text{IR},i}^2 s_\nu^{\text{MS or SB}} \times s_{\nu'}^{\text{MS or SB}} \times n_{ijk}, \quad (\text{B.3})$$

because the fluxes in the two bands are perfectly correlated for sources with the same SED. Finally, we sum over the entire population (all L_{IR} , z , and $\langle U \rangle$) to compute the level of the Poisson term:

$$C_{\ell, \nu \nu'}^{\text{poi}} = \sum_{\{\text{MS, SB}\}} \sum_{L_{\text{IR},i}} \sum_{z_j} \sum_{\langle U \rangle_k} \sigma_{S_\nu S_{\nu'}, ijk}^{\text{MS or SB}}, \quad (\text{B.4})$$

which in integral limit becomes:

$$C_{\ell, \nu \nu'}^{\text{poi}} = \int_z \frac{dV}{dz} \sum_{\{\text{MS, SB}\}} \int_{\langle U \rangle} p_{\text{MS or SB}}(\langle U \rangle | z) \int_{L_{\text{IR}}=0}^{L_{\text{IR},\text{cut}}^{\text{MS or SB}}(\langle U \rangle, z)} \frac{d^2 N_{\text{MS or SB}}}{dL_{\text{IR}}dV} L_{\text{IR}}^2 s_\nu^{\text{MS or SB}}(\langle U \rangle, z) \times s_{\nu'}^{\text{MS or SB}}(\langle U \rangle, z) dL_{\text{IR}} d\langle U \rangle dz. \quad (\text{B.5})$$

Appendix C: Star formation efficiency in the case of a Salpeter IMF

In Sect. 9.3, we computed the SFE assuming a Chabrier (2003) IMF. The results are slightly different if we assume a Salpeter (1955) IMF (see Fig. B.1). In this case, the galaxies close to the mass of maximum ISFE form more stars than they accrete baryons and large gas reservoirs are required to allow the secular star-formation in these objects. These reservoirs could have been replenished during the phase of low star-formation efficiency, when the halo was less massive.

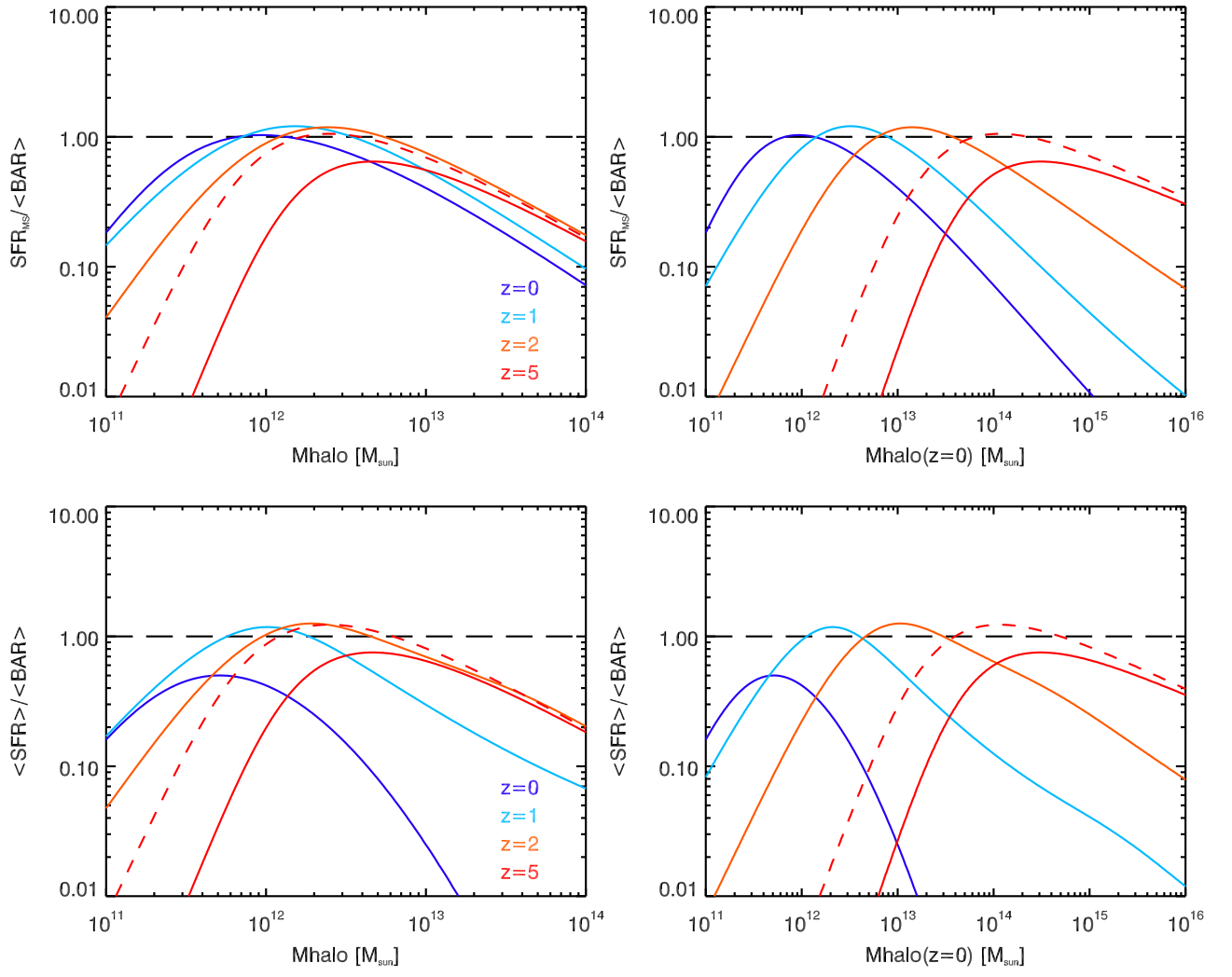


Fig. B.1. Same figure as 16 but assuming a Salpeter (1955) IMF. The black dashed line corresponds to a SFE of 1.